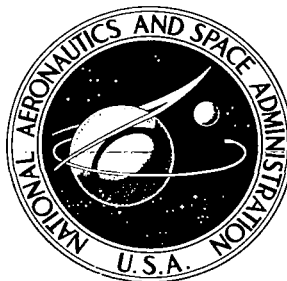


**NASA CONTRACTOR
REPORT**

NASA CR-1353



NASA CR-13

C.1

0060525

TECH LIBRARY KAFB, NM

LOAN COPY: RETURN TO
AFWL (WLIL-2)
KIRTLAND AFB, N MEX

**ONE COMPONENT, MAGNETIC,
SUPPORT AND BALANCE SYSTEM
FOR WIND TUNNEL MODELS**

by K. R. Sivier and M. Henderson

Prepared by

UNIVERSITY OF MICHIGAN

Ann Arbor, Mich.

for Lewis Research Center

NATIONAL AERONAUTICS AND SPACE ADMINISTRATION • WASHINGTON, D. C. • MAY 1969

NASA CR-1353

TECH LIBRARY KAFB, NM



0060525

ONE COMPONENT, MAGNETIC, SUPPORT AND BALANCE
SYSTEM FOR WIND TUNNEL MODELS

By K. R. Sivier and M. Henderson

Distribution of this report is provided in the interest of
information exchange. Responsibility for the contents
resides in the author or organization that prepared it.

Prepared under Grant No. NGR 23-005-003 by
UNIVERSITY OF MICHIGAN
Ann Arbor, Mich.

for Lewis Research Center

NATIONAL AERONAUTICS AND SPACE ADMINISTRATION

For sale by the Clearinghouse for Federal Scientific and Technical Information
Springfield, Virginia 22151 - CFSTI price \$3.00

ABSTRACT

A one-component, magnetic, support-and-balance system was developed to aid in the study of sphere drag at subsonic Mach numbers and Reynolds numbers from about 25 to 4000. This system was used with a vertical wind tunnel and incorporated a simple error-rate type of feedback control system to hold the model vertically. The natural radial stability of the system was used to hold the model on or near the axes of the solenoids and the wind tunnel. The system performed well, especially at Reynolds numbers where unsteady lateral aerodynamic forces were absent or very small.

FOREWORD

This research was part of an investigation, entitled "The Study of the Dynamics of Inert and Reacting Particles in the Exhaust of Solid Rocket Nozzles," that was supported by NASA Grant NsG 86-60. The research was under the technical cognizance of H. Bankaitis, NASA Lewis Research Center, and was conducted at the Gas Dynamics Laboratories, Department of Aerospace Engineering, The University of Michigan, under the direction of Professor J. A. Nicholls.

TABLE OF CONTENTS

	Page
Foreword	iii
List of Illustrations	vi
Nomenclature	vii
Summary	ix
1. Introduction	1
2. System Design	7
2.1 Magnetic System	8
2.1.1 Field Coils; Magnetization of a Sphere	9
2.1.2 Gradient Coil	15
2.2 Magnetic Force Control System	21
3. Calibration and Performance	32
4. Conclusions	39
References	41
Appendix A. Force on a Ferromagnetic Body Immersed in the Symmetrical Field of a Solenoid	67
Appendix B. Helmholtz Field Coil Design	71

LIST OF ILLUSTRATIONS

	Page
Figure 1. Normal and Sheared Magnetization Curves	44
Figure 2. Solenoid Power Factor \overline{M}	45
Figure 3. Solenoid F-Factor Ratio F_3/F_2	46
Figure 4. Solenoid F-Factor F_2	47
Figure 5. Solenoid F-Factor F_1	48
Figure 6. F-Factor Distributions for One and Two Gradient Coil Configurations	49
Figure 7. Block Diagram of Magnetic Force Control System	50
Figure 8. Sketch Showing Model Position Sensor Operation	51
Figure 9. Photograph of Model Position Sensor Assembly	52
Figure 10. Photograph of Model Position Sensing Unit	53
Figure 11. Model Position Sensor Circuit and Output Response to Model Motion	54
Figure 12. Root-Locus Plots for the Magnetic Control System	55
Figure 13. Error-Rate Control Simulation Results; System Response to Step Input	56
Figure 14. Response Using an Error Negation Network; Response to a Step Change in the Position Control	57
Figure 15. Compensation Unit Circuit	58
Figure 16. Current Controller Circuit	59
Figure 17. Photograph of Wind Tunnel with Support-and-Balance System Installed	60
Figure 18. Sketch of Magnetic Coils and Test Section Assembly	61
Figure 19. Gradient Coil Calibration: H_z and $\partial H_z / \partial z$	62
Figure 20. Sketch of Magnetic Model Insertion Probe	63
Figure 21. Load Calibration of Magnetic Support-and-Balance System	64
Figure 22. Control System Transient Response	65
Figure 23. Data from Typical Sphere Drag Test	66
Figure B-1. Helmholtz Pair Geometry	74
Figure B-2. Helmholtz Pair Field and Power Factors	75

NOMENCLATURE

a_i	solenoid inside radius, cm unless otherwise noted
a_o	solenoid outside radius, cm unless otherwise noted
B	magnetic flux density, gauss
B_i	induced flux density, gauss
C_e	error rate coefficient
d	diameter, ft or in.
E	solenoid voltage drop, volts
F	force, dynes
F_1, F_2, F_3	solenoid F-factors, Ref. 27
g	acceleration due to gravity, 980 cm/sec ²
H	magnetic field strength, amp-turn/cm
H_o	empty space solenoid field strength, amp-turn/cm
H_{eff}	effective solenoid field strength in the vicinity of a finite ferromagnetic body, amp-turn/cm
\overline{H}	solenoid power factor, Ref. 12
I	current, amp
I_n	gradient coil current required to support a body with a load factor n , amp
J	current density, amp/cm ²
K_{adj}	compensator gain (adjustable)
K_{cc}	current controller gain
K_s	position sensor gain
ℓ	solenoid winding length, cm unless otherwise noted
m_b	mass of body, gram
M	Mach number, ratio of flow velocity to speed of sound: magnitude of the magnetization vector
\overline{M}	solenoid power factor, Ref. 27

n	load factor; total load divided by the body weight
$N/4\pi$	demagnetization factor of a finite ferromagnetic body
p_o	settling chamber pressure, mm Hg
P	power, watts; differential operator with respect to time, $\partial/\partial t$
q	dynamic pressure, psi
r	radial coordinate, cm
Re	Reynolds number based on diameter, $\rho Vd/\mu$
V	volume, cm^3 ; flow velocity, ft/sec
W	model weight, grams
Y_c	compensator open loop transfer function
Y_o	control system open loop transfer function
Y_s	position sensor open loop transfer function
z	solenoid axial coordinate, measured positive outward from solenoid face, cm unless otherwise noted
Δz	spacing between Helmholtz coil pair, in.
α	winding efficiency coefficient of solenoid
μ	air viscosity, $\text{lb(m)}/\text{ft-sec}$; permeability, henry/m
ρ	air density, $\text{lb(m)}/\text{ft}^3$
ρ_b	mass density of model material, gram/cm^3
ρ_c	electrical resistivity, ohm-cm
τ	control system time constant, sec
τ'	time constant of integrator in control system, sec
ϕ	angle between magnetization vector and solenoid axis, degrees

Subscripts and Superscripts

$(\bar{})$	nondimensionalized by $(a_i)_o$
$()_o$	solenoid face value (at $z = 0$); total or settling chamber value
$()_r$	radial component
$()_z$	axial component

SUMMARY

As part of a study of the drag coefficient of metal oxide particles occurring in rocket motors, it was desired to measure the steady-state drag of spheres (at subsonic Mach numbers and Reynolds numbers below 1000) in a relatively standard way in a wind tunnel. The use of a magnetic support-and-balance system made this possible by (1) eliminating support interference effects and (2) by providing a drag balance with a sensitivity that increases as the model size (and corresponding drag force) decreases. Alignment of the drag and gravity forces by use of a vertical wind tunnel with a downward air flow, allowed the use of a true one-component model support system. This system required only one feed-back control loop to control the upward magnetic force balancing the combined forces of drag and gravity.

The axial magnetic force on a ferromagnetic body, located on the axis of a solenoid, is proportional to the product of the magnetization of the body and the axial magnetic field gradient. In the subject system, a Helmholtz coil pair was used to produce a constant (with time) magnetism of the model. A second, smaller, coil pair was used to produce a small, controllable field gradient (and corresponding magnetic force) sufficient to support the model. The field gradient was controlled by

control of the gradient coil current through a feed-back control loop made up of a model position sensor, a compensator, and a current amplifier in addition to the gradient coils and the magnetic model. The compensator was of the simple error-rate type with a long time constant integrator to reduce the steady-state error of the system.

The support-and-balance system was used in conjunction with a subsonic wind tunnel having a 2-in. diameter test section. The system proved to be simple to use and effective in the study of sphere drag at low Reynolds numbers. For example, with 1/16-in. diameter spheres, drag measurements were made at values of Reynolds number down to about 25; this condition corresponded to a drag force of about 4 milligrams. The low Reynolds number limitation was due to the wind tunnel system and not to the magnetic balance.

The success of a one-component support depends on natural radial stability to keep the model on the solenoid axis. The subject design was found to be satisfactory in this respect for sphere Reynolds number below about 300, where the lateral aerodynamic forces are negligible. At higher values of Re , substantial unsteady, lateral forces occur and under these conditions the one-component system was less satisfactory. However, the natural radial restraint of the support was sufficient to permit good drag measurements at most Re 's up to about 4000; again the limitation was due to the wind tunnel system.

1. INTRODUCTION

The development of a one-component, magnetic support-and-balance system for wind-tunnel models was part of an experimental study of sphere drag¹. This study was concerned with the measurement of sphere drag under flow conditions applicable to the problem of solids-gas flows occurring in the exhausts of rocket motors using metallized fuels. The gas dynamic flow regime experienced by the solid particles in such flows includes Mach numbers from the incompressible up to the low supersonic and Reynolds numbers from a few hundred down to values on the order of unity. In addition, these flows are characterized by high free-stream turbulence. Although the particles can be approximated by spheres, the effect of large surface roughness must be considered.

These flow conditions are very different from those corresponding to standard sphere drag data². In fact, drag data under these flow conditions are scarce and difficult to obtain. The existing data were obtained in free-particle type experiments: e.g., the acceleration of small particles in the flow behind shock waves^{3, 4}, the acceleration and deceleration of particles in steady air streams^{5, 6}, and behavior of a shock wave passing through a solids-gas mixture⁷. It was the objective of the present study to investigate

sphere drag using a fixed-model experimental technique that permitted accurate knowledge and control of the test conditions.

The most obvious experimental technique satisfying this requirement is the continuous wind tunnel. However, this approach has two serious limitations with respect to sphere drag measurements at low Reynolds numbers. Most obvious is the model support interference, which would be expected to be very significant at values of Reynolds numbers where the wake is beginning to form. In addition, the very small drag forces would result in severe problems in the use of a conventional mechanical drag balance.

A search for a suitable experimental approach suggested the use of a magnetic support-and-balance system in conjunction with a small, continuous wind tunnel. The design and operation of magnetic balance systems are well understood and their application to wind tunnel testing is not uncommon. And fortunately, the magnetic balance solves the problems involved in the use of a conventional mechanical support-and-balance system. First, and obviously, the experiment is free of a physical model support. Second, the practical unit of magnetic support force is the weight of the model alone. Since the ratio of aerodynamic force to model weight increases with decreasing model size, one finds that the use of small models

(necessary to achieve small Re) results in high drag forces (in model weight units) and a very sensitive magnetic balance for measuring otherwise very tiny drag forces.

Systems for the magnetic suspension, or levitation, of ferromagnetic bodies are no longer novel. Thirty years ago, F. T. Holmes⁸, at the University of Virginia, devised a system for the stable support of a ferromagnetic needle in the coaxial field of a direct current solenoid. This early system contained all the basic features that are used in the one-dimensional suspension system employed in the present investigation: (1) coaxial fields of direct current solenoids, (2) natural radial stability of the supported body by proper location along the axis of the solenoid, (3) axial stability and position control by an automatic system controlling the current in the solenoid, and (4) an optical sensor for determining the axial position of the supported body.

During the decade following Holmes' original work, Beams et al⁹, also at the University of Virginia, applied the magnetic suspension system to the levitation of spheres that were magnetically spun at high rotational speeds for the study of the phenomena of high centrifugal fields. Later¹⁰ this technique was extended to produce ultracentrifuges with rotor speeds approaching 5×10^7 rpm. Growing out of this work, Beams^{11, 12} developed, in the

early 1950's, a very sensitive magnetic microbalance. In the late 1950's, this same University of Virginia group developed^{13, 14} a three-axis, magnetic support system in which the support forces were automatically resolved into three independent, mutually perpendicular components.

The prospect of the magnetic support of wind tunnel models, thereby eliminating the often troublesome support interference effects, is a very attractive one. However, the magnetic support is basically an unstable one and requires a feed-back control system to provide overall system stability (of course, Holmes already had developed this technique for his one-component system in 1937). In addition, magnetic support systems require almost prohibitive amounts of electrical power, which must be controlled by rapid response control systems, when applied to any but the geometrically smallest wind tunnels. The improvement in the techniques of the control of large quantities of electrical power together with increase in importance of relatively small, high speed wind tunnels finally made magnetic wind tunnel support systems feasible in the 1950's.

Based on the 20 years of experience in magnetic support systems at the University of Virginia, in 1957 Kuhlthau¹⁵ outlined the concept of using Virginia's three-component system as a support and balance for wind tunnel models. However, the French made the first application. Moreau¹⁶ reports

that the application of magnetic support systems to wind tunnel testing grew from work begun at ONERA in France in 1951 on supporting rotating spheres for aerodynamic studies. Although Clemens and Cortner, in their excellent bibliography¹⁷, report that ONERA had magnetically supported wind tunnel models by 1955, the earliest report in the open literature appears to be by Tournier and Laurenceau in 1957¹⁸.

The French system possesses a basic advantage in conventional wind tunnel testing over the three-component Virginia system described by Kuhlthau. It provides for a minimum of five components of force and moment data. This advantage is achieved at the expense of interactions between the several components of magnetic forces and moments and hence presents a basically more complex data reduction problem (a relatively unimportant factor when data reduction is done by modern electronic computers). The modern French "V" system, described by Moreau¹⁶, is a simple development of the early five-component system.

In the United States, MIT has contributed most to development of magnetic support-and-balance systems for wind tunnel models. Their work originally followed the French system and the results of their first studies were reported by Chrisinger in 1959¹⁹. A detailed description of the five-component balance that resulted from these studies is given in Ref. 20.

A far more sophisticated and complex system, providing for a full six components of force and moment data, has been described by Stephens²¹.

The Virginia balance has remained a three-component system. The first use of the balance system resulting from Kuhlthau's work was reported in 1961 by Scott and May²². A complete description of the system itself is given in Ref. 23. A very powerful version of the Virginia balance system has been developed at Princeton University by Zapata and Dukes²⁴. This system, being used in hypersonic wake studies, is capable of supporting aerodynamic loads on the order of 20 times the weight of a spherical model.

The evidence is clear that the use of magnetic support and balance systems is spreading and that the performance of the systems is increasing — at the expense of greater complexity and design sophistication. An excellent view of the state-of-art of (and of the widespread interest in) magnetic systems is provided by Ref. 25.

2. SYSTEM DESIGN

In selecting a configuration for the magnetic support-and-balance system, the principal criteria were simplicity and low cost. Since, initially, the interest was in drag force only, alignment of the drag and gravity force vectors allowed consideration of a true one-component system. In essence, such a system is a simple extension of the 1937-model support system developed by Holmes⁸.

The attainment of a true one-component system is complicated by the fact that the sphere possesses three degrees of freedom. Even when constrained in the flow direction, the sphere can be transversely perturbed, e.g., by free-stream turbulence and/or by an unsteady wake. Holmes showed that it was possible to support a body against the force of gravity with natural horizontal stability, provided that the body was located at the correct point in the field of the solenoid. However, in his initial experiments on supporting a needle and in Beams'⁹ later work on spinning spheres, a provision was made for remote damping of horizontal motions. In the wind tunnel application, the sphere is relatively isolated from its surroundings, i.e., it is located at the center of a wind tunnel test section. Thus, a major unknown was whether or not the sphere would remain near the test section centerline and not be subject to unacceptable horizontal motions.

The support-and balance system consists of two major subsystems: (1) the magnetic system and (2) the control system. These systems have been designed to be compatible with a vertical, subsonic wind tunnel having a 2-in. diameter test section. The magnetic and control systems are discussed in Sections 2.1 and 2.2, respectively, below. The calibration and performance of the support-and-balance system is discussed in Section 3.

2.1 Magnetic System

In Appendix A, it is shown that the axial magnetic force on a ferromagnetic body, located on the axis of a magnetic coil, can be approximated by the expression (where $B_i = \mu M$)

$$F_z \simeq VB_i \frac{\partial H_z}{\partial z} \cos \phi \quad (1)$$

The one-component, support-and-balance system is designed to generate and control this force. If the supported body's intensity of magnetization, B_i , is held constant, a linear relationship exists between $\partial H_z / \partial z$ and F_z . B_i can be held constant either by magnetically saturating the body or by magnetizing the body by a steady, uniform field produced by a coil independent of the coil generating the field gradient. Because of the very large field strengths required to saturate a spherical body magnetically and because of

the very low field gradients needed in the present application, it was decided to base the design of the magnetic system on two separate coils: one to provide a steady, uniform field to magnetize the body and the other to provide sufficient, controllable field gradient for support of the body.

2.1.1 Field Coils; Magnetization of a Sphere

One simple and well known method of producing uniform magnetic fields is by the use of a Helmholtz coil pair. Essentially, the Helmholtz configuration consists of two coils arranged with coincident axes and with a geometry such that the field within a finite volume surrounding the geometric center of the pair is effectively uniform. The characteristics and design of Helmholtz coils with finite winding areas is discussed in Ref. 26. Some of this material is reviewed briefly in Appendix B. In addition, Appendix B presents some charts that are useful in the actual design of Helmholtz coil pairs.

It can be shown²⁷ that the expression for the power absorbed by a coil producing an axial field, H_z , can be written as

$$P = \frac{4\rho_c}{\alpha} (a_i)_o H_z^2 \bar{H} \quad (2)$$

We note here the linear relationship between power and size, $(a_i)_o$. This permits increasing the coil size, and hence the available internal volume

(for location of the gradient coil and the wind tunnel test section) without a great power penalty. On the other hand, the squared dependence of power on field strength, makes the generation of powerful fields costly. Figure B-2 of Appendix B shows that the face diameter ratio \bar{a}_o , of the coils should be fairly large in order to keep the power requirements down. Figure B-1 shows that \bar{a}_o must not be too large if a substantial spacing between the coils is desired: in the present instance, the optical path of the model position sensor must pass between the two field coils.

Based on the above considerations, the following geometry was selected for the Helmholtz field coils:

$$(a_i)_o = 3 \text{ inches}$$

$$\bar{a}_o = 2.09 \quad ; \quad a_o = 6.27 \text{ in.}$$

$$\bar{\ell} = 1.0 \quad ; \quad \ell = 3.0 \text{ in.}$$

$$\bar{\Delta z} = .54 \quad ; \quad \Delta z = 1.62 \text{ in.}$$

$$\bar{H} = 42$$

$$F_1 = 0.5$$

It should be noted that $\bar{\Delta z}$ can be varied substantially from the design point while maintaining field uniformity within an acceptable tolerance. In fact,

a deviation in $\overline{\Delta z}$ can be used in practical applications to increase the size of the acceptably uniform field volume.

The final point to be considered in determining the power requirement of the Helmholtz coils is the field requirement. This, of course, is related to the magnetization properties of the model. The magnetization characteristics of ferromagnetic materials are described by magnetization curves relating the intensity of magnetization B_i (also called intrinsic induction and induced flux density) to the applied field strength H . There are a number of materials that reach magnetic saturation at applied field strengths of a few oersted or less. These materials possess saturated values of B_i in the range from 3000 to 15000 gauss. Unfortunately, this performance occurs only in specimens not affected by the poles set up in the specimens themselves, i. e., rings or infinitely long cylinders. In the case of spheres, the poles are everywhere close to the specimen and have a very strong demagnetizing effect* This effect is described by the relationship

$$H_{\text{eff}} = H_o - \frac{N}{4\pi} B_i \quad (3)$$

*A useful discussion on ferromagnetism, magnetization, magnetic saturation, and demagnetization effects is found in Ref. 28, pp. 1 through 11 and 845 through 849.

where

H_{eff} = effective applied field strength

H_o = applied field strength in the absence of
demagnetizing effects

and

$\frac{N}{4\pi}$ = demagnetization factor

= 1/3, for spheres

Rearranging Eq. (3) for spheres,

$$B_i = 3(H_o - H_{\text{eff}}) \quad (4)$$

Here, H_{eff} is the field strength as it occurs in a normal magnetization curve for an infinitely long specimen. One observes that, until H_{eff} becomes very high (occurs at or above saturation for easily magnetized ferromagnetics), B_i is approximated by the relation

$$B_i \simeq 3H_o \quad (5)$$

Thus for spheres, the use of easily magnetized (and expensive) ferromagnetics generally is not warranted and the magnetization obtained will be nearly independent of the sphere material.

This demagnetization effect made the problem of material selection and model manufacture a trivial one. Precision ball bearings, made of weakly

magnetic Type 440C stainless steel, are commercially available. The sheared (refers to a finite specimen, here a sphere) magnetization curve for this material is compared with its normal magnetization curve and the sheared curve for easily magnetized (saturated at an applied field strength on the order of 10 oersted) Allegheny Ludlum electrical steel 4750 in Fig. 1.

The final design of the coils represented a compromise between available conductor materials, cooling requirements, and the desire to achieve as high a value of B_1 as possible. The conductor material selected was 1/4-in. O.D. by 0.030-in. wall copper tubing with a 1/32-in. thick polyvinyl chloride (PVC) insulating sheath. The geometry of this conductor gives a maximum value of the winding efficiency factor α of about 0.2. Manufacturer's data on this tubing showed that it could be used at pressures up to about 500 psi and temperatures up to about 200⁰F.

Cooling water is supplied by a 500 psi, 2 gpm pump. This performance is matched to the 500 psi pressure drop across each coil at a flow rate of 1 gpm; the coils are connected in parallel for cooling purposes.

Power is supplied by the Gas Dynamics Laboratories' DC power supply. This power supply can provide up to 1200 amps at 120 volts, with either the current or voltage output automatically controlled. This power supply is

nearly ideal for powering the field coils, except for a substantial ripple in its output, especially at low current levels.

A check of the power dissipation in the Helmholtz pair showed that an input of about 15 KW would be required for a 2000 oersted field and about 34 KW for a 3000 oersted field. At a water flow rate of 1 gpm through each coil, these powers correspond to cooling water temperature rises of about 50 and 115⁰F, respectively. The latter temperature rise gives an average outlet water temperature of about 165⁰F. This was considered to represent a working maximum to insure that the PVC insulation did not exceed its 200⁰F maximum working temperature. It therefore appeared that the field would have to be limited to a maximum of 3000 oersted (corresponding to a B_i of a sphere of about 8300 gauss).

A final point of interest was the current to be carried by the conductor and total voltage drop occurring across the two coils connected electrically in series. Based on the selected geometry and the above power calculations, the estimated electrical characteristics of the coil are as follows:

H _z , Oersted	2000	3000
P, KW	15	34
J, amp/in. ²	2700	4000
I, amp	260	390
E _{total} , volts	58	87

These values fall well within the capabilities of the DC power supply.

2.1.2 Gradient Coil

In addition to the obvious requirement of producing a large enough field gradient to provide the necessary magnetic force, the gradient coil was designed to meet two other objectives; i.e., low input power and high radial stability of the model. It can be shown²⁷ that the power required for the gradient (levitating) coil can be written as

$$P = 3.842 \times 10^8 \frac{n^2}{\alpha} \rho_c (a_i)_o^3 \left(\frac{\rho_b}{B_i} \right)^2 \bar{M} \quad (6)$$

and the radial stability derivative of the body as

$$\frac{1}{m_b} \frac{\partial F_r}{\partial r} = -4.9 \times 10^2 \frac{n}{(a_i)_o} \left(\frac{F_3}{F_2} \right) \quad (7)$$

where \bar{M} and F_3/F_2 are non-dimensional magnetic field factors that are determined by the coil geometry, but not its scale. The evaluation of these factors is discussed in detail in Ref. 27; Figs. 2 and 3 illustrate the variation of these factors with the geometric parameters \bar{a}_o , $\bar{\ell}$, and \bar{z} .

The axial magnetic force acting on a ferromagnetic body can be written as²⁷

$$F_z = -0.05 V B_i J F_2 \cos \phi \quad (8)$$

where F_2 is a dimensionless factor that depends on the geometry of the coil-body system and is related to the field gradient through the equation

$$\frac{\partial H_z}{\partial z} = -\frac{1}{2} J F_2 \quad (9)$$

The variation of F_2 with \bar{a}_o , $\bar{\ell}$, and \bar{z} is illustrated in Fig. 4. In general, there are two axial positions, relative to the face of the coil, where the field gradient is of the correct magnitude to produce the desired magnetic force. However the equation for radial stability above shows that the ratio F_3/F_2 must be positive and Fig. 3 shows that positive values of F_3/F_2 occur only near the coil face. Furthermore, radial stability increases as the coil face is approached. In a magnetic support system such as this, radial and axial stabilities of the supported body are mutually exclusive. In fact for this system, it is found (Ref. 27) that

$$\frac{\partial F_r}{\partial r} = -\frac{1}{2} \frac{\partial F_z}{\partial z} \quad (10)$$

Thus, a design based on achieving natural radial stability results in a system that is axially unstable. Overcoming this axial instability is an added requirement for the control system described in Sec. 2.2 below.

Figure 2 shows that, from an input power standpoint, the coil should not be too short (small $\bar{\ell}$) for small \bar{z} 's and that the coil face diameter ratio,

\bar{a}_o , should be fairly low. As a compromise between the requirements of model radial stability, input power, and available space, the following geometry was selected for the gradient coil:

$$\bar{a}_o = 1.5$$

$$\bar{\ell} = 0.5$$

$$\bar{z} = \text{practical minimum depending on model diameter and optical sensor characteristics.}$$

and based on a \bar{z} of 0.1,

$$F_2 \simeq .11$$

$$\bar{M} \simeq 170$$

The axial field produced on the axis of a coil can be calculated from the relation²⁷

$$H_z = \frac{1}{2} J(a_i)_o F_1 \quad (11)$$

The variation of the dimensionless factor F_1 with \bar{a}_o , $\bar{\ell}$, and \bar{z} is illustrated in Fig. 5. Based on the geometry selected for the gradient coil

$$F_1 = 0.18$$

Inspection of Eqs. (6) and (7) above shows the desirability of keeping the gradient coil size, characterized by the inner radius $(a_i)_o$, as small as possible. The wind tunnel test section, used with this coil, has an outside

diameter of 2 1/2 in. Allowing some clearance between the test section and gradient coil, a coil inside diameter of 3 in. was chosen so that $(a_1)_0 = 1.5$ in.

One further refinement was made in the design of the gradient coil. The field produced by the gradient coil changes with the load on the model and, hence, the magnetization of the model will change with the load. This tends to upset the desired linearity between field gradient and magnetic force. If instead of one gradient coil, two gradient coils with opposing fields are used, then the field due to the gradient coils will be smaller and the effect on the model's magnetization will be decreased. An additional benefit occurs because the field gradients are additive when the fields are in opposition. The result of this gradient addition is that each of the two coils needs to supply only about one-half of the total required gradient and, hence, the power requirement of each coil is reduced by a factor of about four: the total power required for the two coils is about one-half that required by a single coil. This, in addition, greatly reduces the coil heating problem; each coil is receiving only one-quarter of the power received by a single coil. In the present case, this decrease was enough to eliminate the need for coil cooling; a very great simplification indeed.

The principal disadvantage of the two-coil configuration lies in a decrease in radial stability. Even though the contributions to the F-factors F_2 and

F_3^{27} are additive near the face of the primary coil, the stability-related ratio, F_3/F_2 , is decreased everywhere between coils.* The result is about a 40% reduction in radial stability for the 1-in. coil spacing used.

In Fig. 6, the distributions of F_1 , F_2 , and F_3/F_2 along the coil axis are compared for the single and double coil configurations. It is interesting to observe that midway between the coils, the field decreases to zero (as does the radial stability) while the gradient is a maximum. This would be an ideal model location for a 3-component support system where the radial stability is provided by the control system.

Using Eq. (6) and noting that each coil is providing approximately one-half of the necessary gradient, the power per coil required to support a steel sphere is ($\rho_c = 1.6 \times 10^{-6}$ ohm-cm, $\rho_b = 8$ gram/cm³):

H_z , oersted	B_1 , gauss	P, watts per coil
2000	5700	4.0
3000	8400	1.8

*Note that in determining the ratio F_3/F_2 for the two coil configuration, the F_3/F_2 contributions of the individual coils cannot be added. Rather, the F_2 and F_3 contributions of the individual coils are summed and the F_3/F_2 ratio is formed from these total values.

These power values are based on copper wire conductor. The winding area efficiency factor, α , for wire is about 0.7, allowing for about a 10% winding loss from the geometric maximum α .

The coils were wound from No. 20, single filament, cement coated magnet wire. After baking, this winding is self-supporting and eliminates the need for a support arbor. Use of No. 20 wire resulted in a resistance of about 4.5 ohms per coil. On this basis, the current through the gradient coils and the voltage drop across the pair (connected in series) was calculated to be

H_z , oersted	I, amperes	E, total volts
2000	0.95	8.5
3000	0.63	5.7

The overall performance criterion for the support system was the support of total loads four times the model weight ($n = 4$). The relationship between magnetic force and coil current (and voltage drop) is linear. Introducing the force required to support a body with a load factor n into Eq. (8), the required current density becomes

$$J = - 1.96 \times 10^4 \frac{n\rho_b}{B_i \cos \phi} \frac{1}{F_2} \quad (12)$$

On the basis of Eq. (11), the conservative maximum operating condition for the gradient coils and for the gradient coil current controller was established as

$$I = 4 \text{ amp}$$

$$E = 35 \text{ volts}$$

2.2 Magnetic Force Control System

As pointed out in the introduction to Section 2.1 above, the magnetic support-and-balance system is based on the separation of the model magnetization, B_i , and the field gradient, $\partial H_z / \partial z$, factors in the force equation

$$F_z \simeq V B_i \frac{\partial H_z}{\partial z} \cos \phi$$

B_i is held nominally constant by the Helmholtz field coil pair described in Section 2.1.1 above. Thus, control of the magnetic force is achieved through control of $\partial H_z / \partial z$, generated by the gradient coil pair discussed in Section 2.1.2 above. Noting that for a given coil the winding current density J is proportional to the conductor current I , the magnetic force equation, Eq. (8), can be written as

$$F_z \propto V B_i I F_2$$

Thus, F_z varies linearly with I provided that both B_i and F_2 are held constant. F_2 depends only on the geometry of the gradient coils and, for a given set of coils, only on the axial position of the model relative to the coils (see Fig. 6). This suggests that, in addition to providing control of the magnetic force so that the model is stably supported, it is desirable for the control system to keep the model fixed in space.

The axial force on the supported body is a function of the axial model position z and the gradient coil current I . Thus, if it is assumed that the control system controls I as a function of z , $I = I(z)$, then the total stability derivative has the form

$$\frac{dF_z}{dz} = \left(\frac{\partial F_z}{\partial z} \right)_I + \left(\frac{\partial F_z}{\partial I} \right)_z \frac{dI}{dz}$$

Since the body/coil geometry of the present design results in static axial instability, $(\partial F_z / \partial z)_I > 0$, overall axial stability requires that

$$\left(\frac{\partial F_z}{\partial I} \right)_z \frac{dI}{dz} < - \left(\frac{\partial F_z}{\partial z} \right)_I$$

Furthermore, the system geometry results in

$$\left(\frac{\partial F_z}{\partial I} \right)_z > 0$$

so that axial stability requires that

$$\frac{dI}{dz} < - \frac{(\partial F_z / \partial z)}{(\partial F_z / \partial I)} \frac{I}{z}$$

Thus the control system must sense the body's position and appropriately vary the gradient coil current so that the above requirement is met. This is accomplished by a closed loop, feed-back system that includes, in addition to the magnetic body and the gradient coils, (1) a model position sensor, (2) a compensator, and (3) a gradient coil current controller. A block diagram, showing the relationship of the several system components, is presented in Fig. 7.

The model position sensor detects the position of the model by a beam splitting technique and generates a voltage signal proportional to the model's deflection from some desired position. The arrangement of the model position sensor is sketched in Fig. 8. Figure 9 presents a photograph of sensor components mounted on the support ring. A close-up of the sensing unit is shown in Fig. 10. The light from a flashlight bulb is collected by the collimating lens, is projected through the wind tunnel test section windows, and falls on the light mask. The light that passes the mask is refocused and then split horizontally by a 45° prism. The two beam halves fall on light

sensors located near the focal points. The light sensors are Texas Instruments Photovoltaic cells. These cells are current sources and their output is a linear function of the light energy incident on the sensitive surface of the sensor. The output circuits of the two sensors are arranged, as shown in Fig. 11, so that the net output voltage is zero when each sensor receives the same light input.

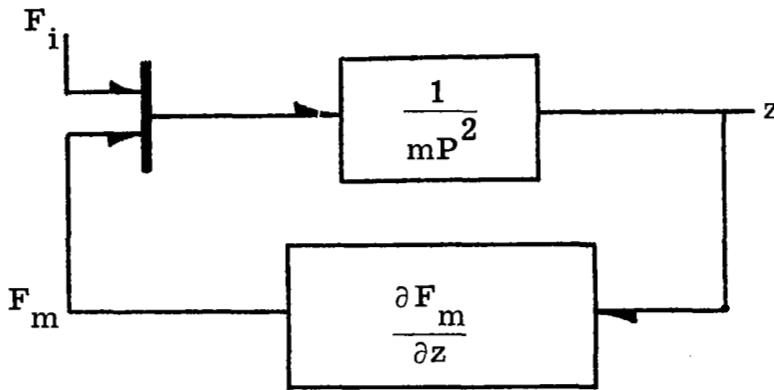
In operation, the prism is adjusted so that the voltage outputs of the light sensors are equal; this is roughly equivalent to splitting the incident beam in half. When a supported sphere is located so that its shadow is split in half by the prism, the outputs of the sensors are still equal; this is the null position for the sphere. As the sphere moves from its position in the center of the light beam, it increases the amount of light incident on one sensor and decreases the amount of light on the other. This produces a net voltage that is roughly proportional to the deviation of the model from its initial position; the voltage polarity indicates the direction of sphere motion.

The opening in the light mask is equal to or slightly greater than the sphere diameter in height and is equal to or greater than three diameters in width. This large horizontal dimension permits the sphere to move laterally without affecting the vertical control performance. With this geometry, the model in either of its extreme positions blocks approximately

30% of the total light input to the corresponding sensor. Typically the position sensor generates about 350 millivolts with the model in an extreme position. The transfer function, Y_s , for the position sensor is defined by

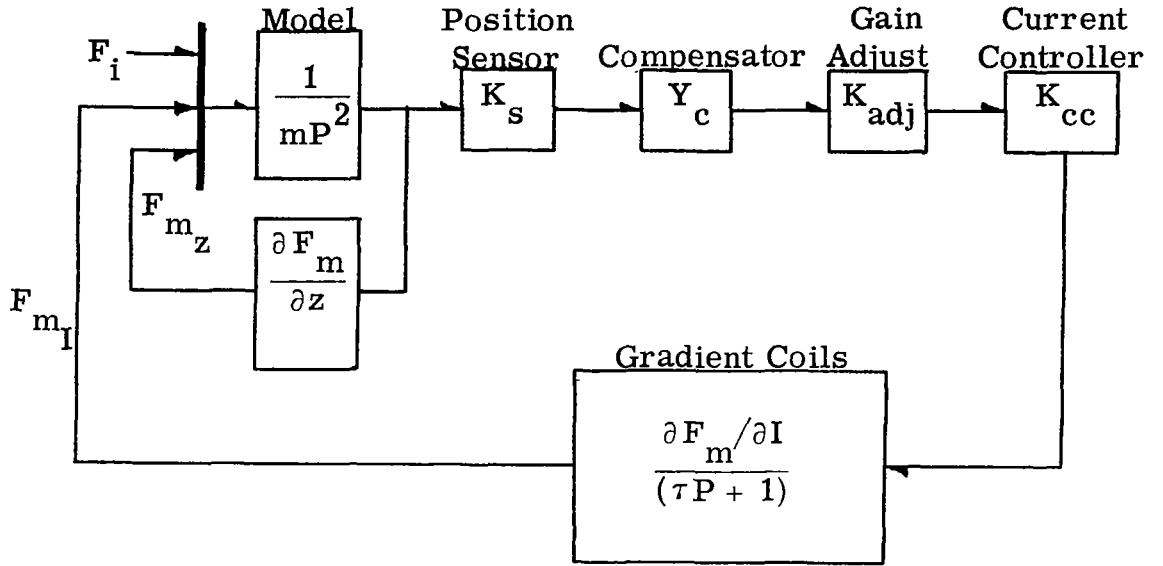
$$V_e = Y_s \Delta z$$

The dynamics of the sphere (in vertical motion) are indicated by the following diagram.



In this diagram, F_i is the sum of the gravity and drag forces and F_m is the magnetic force produced at a fixed current in the gradient coils.

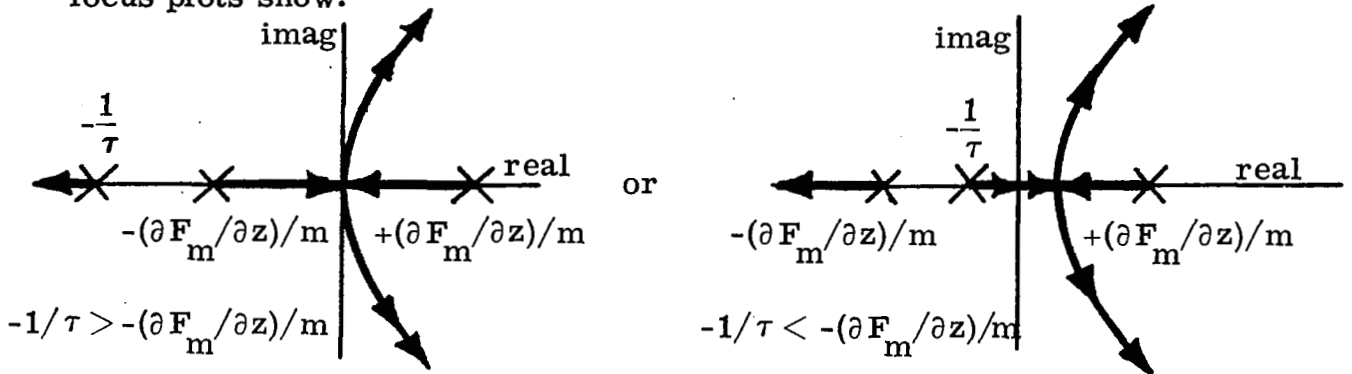
With the addition of the sphere dynamics, the diagram for the entire control loop becomes:



Here it is assumed that the coils are a pure time lag and that the position sensor and the current controller are amplifiers with zero time lags (thus, $Y_s = K_s$). Y_c is the transfer function of the compensator and determines how the current in the gradient coils changes in response to model motion. It is this transfer function, as was mentioned previously, that must produce the system's stability. Trying the simplest control scheme first, simple proportional control (i. e. , $Y_c = \text{const}$) was investigated. For simple proportional control, the open loop transfer function is

$$Y_o = \frac{(K_s) (K_{adj}) (K_{cc}) (Y_c) \left(\frac{\partial F_m}{\partial I} / m \right)}{\left(P + \frac{\partial F_m}{\partial z} / m \right) \left(P - \frac{\partial F_m}{\partial z} / m \right) (\tau P + 1)}$$

However, this loop proved to be unstable, as the following sketches of the root-locus plots show.



These sketches are qualitative, but they show that the locii of the roots of Y_o are never all in the left half plane. Thus, the system is unstable for any gain.

While the investigation of simple proportional control was somewhat academic, it provided an analytic starting point and indicated a need for lead elements in the compensator. With this in mind, an error-rate compensator was investigated as the next least complicated controller. The error-rate transfer function

$$Y_c = \frac{C_e P + 1}{.1C_e P + 1}$$

was chosen for initial analysis because it is a practical circuit that can easily be built of standard analog computer components. For this controller, the system's open loop transfer function is

$$Y_o = \frac{\left[(K_s) (K_{adj}) (K_{cc}) \left(\frac{\partial F_m}{\partial I} / m \right) \right] \left(P + \frac{1}{C_e} \right)}{(\tau) (.1) \left(P + \frac{1}{\tau} \right) \left(P + \frac{10}{C_e} \right) \left(P + \frac{\partial F_m}{\partial z} / m \right) \left(P - \frac{\partial F_m}{\partial z} / m \right)} \quad (13)$$

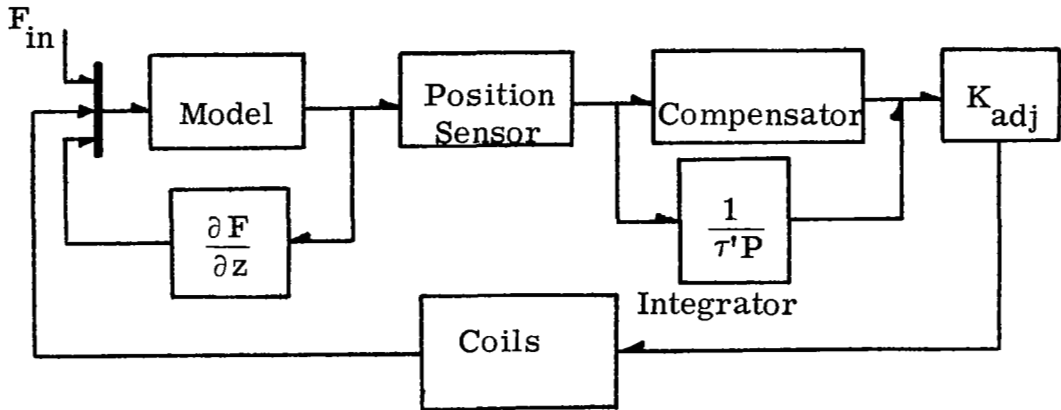
Root locus plots for this transfer function were made for several values of C_e and indicated that the simple error-rate controller would provide excellent response and damping if the coil lags are kept low. For a C_e of .1, the analysis showed that coil lags of up to 10 ms can be tolerated. Since the coils built for this system had a measured inductive time constant of only 1 ms, the error-rate controller was considered acceptable. The root-locus plots presented in Fig. 12 show the effect of coil time lags on an error-rate controller. The open loop transfer function is that given by Eq. (13) and $C_e = .1$. The model was assumed to be a 1/16 in. diameter steel ball bearing.

Figure 12 shows that as the time lags increase, the off-axis root crosses into the right half-plane at progressively lower gains. At $\tau = 10$ ms this gain is 2100, just a little higher than the minimum gain required to bring the on-axis root into the stable left half-plane. This would be the neutrally stable case since the damping is nearly zero. For $\tau = 20$ ms the off-axis root crosses over at a gain of 1850 as shown in Fig. 12; this is not enough gain

to pull the on-axis root into the right half-plane, and the system is unstable. For a system with $\tau = 1$ ms, the effect of the lag is small and the system may be satisfactorily approximated by letting $\tau = 0$.

To check the mathematical analysis of this control loop and to determine the desired values of C_e and the total loop gain, the entire loop (for $\tau = 0$) was simulated on an analog computer. Typical results are shown in Fig. 13. These results verified the analysis of the system's stability. Under steady-state conditions, a simple error-rate controller has an output that is directly proportional to the input error. In the wind tunnel model support situation, this type of performance results in model sag (movement toward the principal coil face) as the aerodynamic load increases. The simulation results (e.g., Fig. 13) showed that the steady state position error for the system as designed was of the order of 1/10th ball diameter per g of load. This model sag would cause nonlinearities in the system's load response curve (F_z vs. I), since, as we have seen, the magnetic force on the model is a function of vertical position as well as field gradient. Although such nonlinearities are acceptable as long as they are consistent, they are a nuisance and make data reduction difficult. For this reason an error-negation network was added to the system. This network consists of an integrator with a high time constant which integrates the error signal and

introduces the resulting signal back into the system. The time constant of this integrator is 0.1 sec; this is about two orders of magnitude greater than the time constant of the rest of the control loop and, hence, the system's dynamics are essentially independent of the presence of the integrator. The control loop with the integrator becomes:



This loop was also simulated for $\tau' = .1$ sec and the results are shown in Fig. 14.

The compensator and integrator units were assembled using Philbrick P65AU operational amplifiers. Figure 15 shows the amplifier arrangement and the components used to produce error-rate control with $C_e = .1$ and an integrator time constant τ' of .1 sec.

Figure 16 shows the current controller circuit. This circuit is basically a PNP preamplifier coupled to a two-stage Darlington circuit, the last

stage of which controls the current in the gradient coils. The output stage of the current controller regulates the coil current from zero to 4 amps. The power is supplied by a 48 V, 6 amp, DC power supply with about 5% ripple at 120 cps. The current response of this circuit to signal input from the compensator is about 3.5 amps/volt with a rise time of less than 10 microseconds.

3. CALIBRATION AND PERFORMANCE

A photograph of the wind tunnel, with the support-and-balance system installed, is presented in Fig. 17. Details of the geometric arrangement of the coils, wind tunnel test section, and the model are shown in Fig. 18. Also shown are the directions of the induced magnetization B_i , the field gradient, and the forces acting on the model; positive z is taken upward, measured from the upper face of the lower or principal gradient coil. Because of space requirements for the position sensor ring and the arbor end plates, the Helmholtz coils are separated by 2 in. rather than by the design spacing of 1.62 in. The gradient coils are spaced 1 in. apart with the lower coil face slightly below the position sensor axis which passes through the window centers.

As mentioned earlier, the Helmholtz coils are powered by the Laboratories' DC power supply. The current output of the power supply is controlled remotely by a portable control station that is positioned adjacent to the wind tunnel. The coils are protected from overheating due to loss in water pressure by a pressure switch in the cooling water supply line that is interconnected with the power supply control. Instrumentation for the field coils consists of:

1. Voltmeter measuring the voltage drop across the coils.
2. Ammeter measuring the coil current.
3. Brown recorder giving a continuous record of the coil current.
4. Thermocouple and meter measuring the PVC insulation temperature near the cooling water outlet.
5. Pressure gauge measuring the cooling water inlet pressure.

The only instrumentation used with the gradient coils is a Brown recorder that measures the current in the gradient coil circuit.

A Bell "120" gaussmeter was used to measure the field strength and distribution of the two pairs of coils. At their geometric center, the Helmholtz coils were found to generate 7.55 oersted per ampere. Thus, a 2000 oersted field requires a 265 ampere current, compared to the design value of 260 amperes. The voltage drop across the coils, at this current, is about 60 to 65 volts, compared to the design estimate of 58 volts. No detectable field variation was found within a 1-in. radius of the center of the coils, verifying the effectiveness of the Helmholtz design and justifying the greater than design separation between the coils.

The measured field distribution, between the gradient coils, and the resulting field gradient distribution are shown in Fig. 19. These data were obtained with a coil current of 0.8 amperes. Thus the gradient coil field in the vicinity of the model is about 25 oersted per ampere, opposing the

field due to the Helmholtz coils. This results in a decrease in B_i of about 1% per g of model load for a Helmholtz field of 2000 oersted or about 0.5% per g for a 3000 oersted field.

The static performance of the system was verified by demonstrating the linearity between the force on the model and the gradient coil current. This was done through a static load calibration of the balance. It should be noted that the system is calibrated automatically at one point each time it is used. Each test is begun by levitating the model alone in still air. This determines the coil current required to produce a magnetic force equal to one model weight, i. e., 1 g.

The spherical models were inserted into the system by means of the probe shown in Fig. 20. This probe was held in a jig, located above the coils, that permitted precise positioning of the model. The magnetic field of the Helmholtz coils magnetized the steel rod sufficiently to hold the model tightly against the non-magnetic tip; the rod was positioned so that it did not touch the model. The probe was lowered until the model just touched the part of the control system's light beam that passes through the light mask and the model was released by withdrawing the steel rod from the probe. The slowly falling model was easily caught and held by the magnetic support system.

The calibration procedure was as follows. A fine thread, with a loop at one end, was cemented to a sphere and the whole assembly weighed in a precision balance, as was the sphere before attaching the thread. Then the sphere with the attached thread was levitated. Finally, carefully weighed pieces of non-magnetic wire were hooked to the loop to "load" the system. The practical unit of weight in this system is the weight of the sphere alone. Therefore, the load factor n (the total weight of the sphere, string, cement, and attached weights divided by the weight of the sphere alone) was taken as the loading unit. Figure 21 presents the results of two typical system calibrations in the form of the gradient coil current ratio, $(I_n - I_{n_0})/I_{n=1}$ where I_{n_0} is the current required to support the sphere plus thread and cement, as a function of incremental load factor, $n - n_0$.

These results show a small nonlinearity in the system. Part of this is due to the 1% decrease in B_i per sphere weight of load referred to above. The remainder is due to a nonlinear model sag under load, resulting in a decreasing field gradient with load; an indication of the inability of the integrating circuit to remove the entire steady-state position error due to loading. This sag can be decreased by increasing the gain of the compensator. However, the system becomes unstable at high gains; the results presented in Fig. 21 are for the highest practical gain setting for each sphere size.

Two simple tests were made to demonstrate the dynamic response characteristics of the system. In the first, a small non-magnetic weight was dropped onto a suspended sphere. This weight bounced off the sphere and effectively produced an impulse load input to the system. The response of the system to this type of load is shown by the oscilloscope picture presented in Fig. 22(a). This trace shows good system dynamic stability with a natural frequency (with the 1/4-in. diameter sphere used in this test) of about 26 cps. The oscillations damp out in about 100 msec and the sphere returns to its initial position in about 135 msec. In the second test, a 1/8 g weight was dropped onto the loading loop of a suspended sphere. This produced a step load input. The response is indicated by Fig. 22(b). Note the decreased sweep rate and reversed polarity used for this oscilloscope picture. In this case the sphere motion is arrested in about 100 msec and the integrator requires about another 250 msec to return the sphere to its initial position. Again the system exhibits satisfactory dynamic response.

The sphere drag data obtained with this support-and-balance system are discussed in Ref. 1 and 29. Some typical data from this investigation are shown in Fig. 23. This figure shows the dimensionless drag force (load factor $n - 1$) versus the tunnel stagnation pressure for $M = 0.16$. The drag force, $n - 1$, was determined from the measured gradient coil current on

the basis of the relationship

$$n - 1 = \frac{(I)_{\text{wind-on}}}{(I)_{\text{wind-off}}} - 1$$

Figure 23 also shows the drag force reduced by the dynamic pressure, q . This ratio, $(n - 1)/q$, is proportional to the drag coefficient. These data cover the Reynolds number range from about 50 to 1500. The data shown in Fig. 23 are typical with respect to the small scatter and good repeatability that was achieved with the system.

An interesting feature of this system is its ability to measure the very small drag forces acting on small spheres at low Reynolds numbers. In the subject investigation, drag measurements were made with 1/16-in. diameter spheres at values of Re down to about 25. The corresponding drag force was about 4 milligrams. The weight of the 1/16-in. sphere was about 16 milligrams; the 4 milligram force represented a 1/4 g drag load. Tests at lower values of Re were precluded by the operating limitations of the wind tunnel system. However, experience with larger spheres (at larger Re 's) showed the balance provided good data for loads down to about 0.1 g. Thus measurement of drag loads of 2 milligrams or less should be possible with 1/16-in. spheres*

*Attempts to use spheres smaller than 1/16-in. were unsuccessful. It was thought that this was caused by the inability of the model position sensor to "see" the shadow of such small spheres. Improvements in the position sensor optics should permit the use of smaller spheres.

Radial stability was found to be an important factor in the operation of the support-and-balance system. Below a Reynolds number of about 300 ($p_o < 18$ mm Hg in Fig. 23), the flow about the sphere is essentially steady and the model is subject to no lateral disturbances (for a low-turbulence free stream). Under these conditions, the models were found to remain almost motionless at the test section center. However at higher Reynolds numbers ($Re_d > 300$), the unsteady sphere wake produced large lateral force fluctuations. These force fluctuations caused the model to oscillate laterally; sometimes with sufficient amplitude to drive the model outside the control system's light beam, resulting in loss of the model. Under this condition of the fluctuating lateral forces, the natural radial stability of the system was insufficient. In spite of this, the data taken at these higher Reynolds numbers did not exhibit deleterious effects of the lateral model motion.

4. CONCLUSIONS

This investigation has demonstrated the practicality of the use of a one-component, magnetic support-and-balance system in the study of sphere drag. This technique was found to be particularly valuable at low sphere Reynolds numbers where the use of small spheres is advantageous. Under these conditions, the magnetic support system eliminates support interference effects and the balance sensitivity increases as the sphere size (and the corresponding drag force) decreases.

The one-component system provides model position control only along the wind axis. Thus, satisfactory operation depends on the natural radial stability of the system to restrain the model in the two lateral degrees of freedom. The one-component system was found to be completely satisfactory at Reynolds numbers below 300 where flow about the sphere produces no lateral force fluctuations. However, at higher Reynolds numbers, the unsteady separated flow at the rear of the sphere and the fluctuating wake produced fluctuating lateral forces that caused substantial lateral motion of the sphere. In some cases, the motion was sufficient to cause loss of the model. For such test conditions, support operation would be substantially improved by the addition to controlled lateral restraint to aid in holding the model in a fixed position.

Finally, the simplicity and relatively low cost of the one-component system were demonstrated. With a magnetizing field of about 2000 oersted, it was possible to support stainless steel spheres with gradient coil currents of about one ampere per g of force on the sphere. Thus the gradient coil current controller was required to handle at most a few amperes. Because of the large demagnetization effect of the spherical shape, the 2000 oersted field was able to magnetize the ferromagnetic spheres only to about 40% of the saturated value. The availability of a 7000 oersted field would have saturated the spheres magnetically and reduced the gradient coil current requirement by about 60%.

REFERENCES

1. Sivier, K.R., "Subsonic Sphere Drag Measurements at Intermediate Reynolds Numbers," Ph.D. Thesis, The University of Michigan, 1967.
2. Schlichting, H., Boundary Layer Theory, 4th ed., McGraw-Hill Book Co., Inc., 1960, p. 16.
3. Crowe, C.T., "Drag Coefficients of Inert, Burning, or Evaporating Particles Accelerating in Gas Streams," Ph.D. Thesis, The University of Michigan, 1961.
4. Selberg, B.P., "Shock Tube Determination of the Drag Coefficient of Small Spherical Particles," (University of Michigan), NASA CR 418, April, 1966.
5. Ingebo, R.D., "Drag Coefficients for Droplets and Solid Spheres in Clouds Accelerating in Airstreams," NACA TN 3762, September, 1956.
6. Torobin, L.B. and Gauvin, W.H., "The Drag Coefficients of Single Spheres Moving in Steady and Accelerated Motion in a Turbulent Fluid," A.I.Ch.E. J., Vol. 7, No. 4, December, 1961.
7. Rudinger, G., "Experiments on Shock Relaxation in Particle Suspensions in a Gas and Preliminary Determination of Particle Drag Coefficients," Cornell Aeronautical Laboratory, Project SQUID Tech. Rept. CAL-90-P, July 1963.
8. Holmes, F.T., "Axial Magnetic Suspensions," Rev. Sci. Inst., Vol. 8, November, 1937, p. 444.
9. Beams, J.W., Young, J.L., and Moore, J.W., "The Production of High Centrifugal Fields," J. App. Phys., Vol. 17, November 1946, p. 886.
10. Beams, J.W., "Magnetic-Suspension Ultracentrifuge Circuits," Electronics, March 1954, p. 153.
11. Beams, J.W., "Magnetic Suspension Balance," Phys. Rev., Vol. 78, 1950, p. 471.

12. Beams, J.W. et al, "Magnetic Suspension Balance," Rev. Sci. Inst., Vol. 26, 1955, p. 1181.
13. Jenkins, A.W. and Parker, H.M., "Electromagnetic Support Arrangement with Three Dimensional Control - I. Theoretical," J. App. Phys., Supplement to Vol. 30, No. 4, April 1959, p. 238S.
14. Fosque, H.S. and Miller, G.H., "Electromagnetic Support Arrangement with Three-Dimensional Control - II. Experimental," J. App. Phys., Supplement to Vol. 30, No. 4, April 1959, p. 240S.
15. Kuhlthau, A.R., "The Investigation of Low Density Drag Phenomena Utilizing Laboratory Techniques," Proc. Fourth U.S. Navy Symp. on Aeroballistics, November 12-14, 1957.
16. Moreau, R., "Use of Magnetic Suspension System in ONERA Wind-Tunnel," Summary of ARL Symposium on Magnetic Wind Tunnel Model Suspension and Balance Systems, USAF OAR Rept. ARL 66-0135, July 1966, p. 199.
17. Clemens, P.L. and Cortner, A.H., "Bibliography: The Magnetic Suspension of Wind Tunnel Models," USAF Rept. AEDC-TDR-63-20, February 1963.
18. Tournier, M. and Laurenceau, P., "Suspension Magnetique d'une Maquette en Soufflerie," (Magnetic Suspension of a Model in a Wind Tunnel), ONERA La Recherche Aeronautique, No. 59, July-August 1957, p. 21.
19. Chrisinger, J.E., "An Investigation of the Engineering Aspects of a Wind Tunnel Magnetic Suspension System," Aeronautical Engineering Degree Thesis, Massachusetts Institute of Technology, June 1959 (also MIT TR 460, May 1959).
20. Tilton, E.L. et al, "The Design and Initial Operation of a Magnetic Model Suspension and Force Measurement System," (MIT) USAF OAR, ARL 63-16, January 1963.
21. Stephens, T., "The General Features of a Six-Component Magnetic Suspension and Balance System," (MIT), Summary of ARL Symposium on Magnetic Wind Tunnel Suspension and Balance Systems, USAF OAR, ARL 66-0135, July 1966, p. 81.

22. Scott, J.E., Jr. and May, J.E., "Laboratory Investigation of the Basic Nature of Low Density Gas Flow at High Speeds," Univ. of Virginia Res. Labs for the Engrg. Sciences Rept. No. AST-4435-109-61U, January 1961.
23. Parker, H.M., May, J.E., and Nurre, G.S., "An Electromagnetic Suspension System for the Measurement of Aerodynamic Characteristics," Univ. of Virginia Res. Labs for the Engrg. Sciences Rept. No. AST-4443-106-62U, March 1962.
24. Zapata, R.N. and Dukes, T., "An Electromagnetic Suspension System for Spherical Models in a Hypersonic Wind Tunnel," Princeton Univ. Dept. of Aero and Mech. Sciences Rept. 682, July 1964.
25. Daum, F.L. (ed.), "Summary of ARL Symposium on Magnetic Wind Tunnel Model Suspension and Balance Systems," USAF OAR Rept. ARL 66-0135, July 1966.
26. Franzen, W., "Generation of Uniform Magnetic Fields by Means of Air-Core Coils," Rev. Sci. Inst., Vol. 33, No. 9, September 1962, p. 933.
27. Sivier, K.R., "Magnetic Field Properties Related to the Design of a One-Component Magnetic Support-and-Balance System," NASA CR-1352, 1969.
28. Bozorth, R.M., Ferromagnetism, D. Van Nostrad Co., Inc., 1951.
29. Sivier, K.R., "Subsonic Sphere Drag Measurements at Intermediate Reynolds Numbers," (University of Michigan), NASA Contractors Report (in preparation).

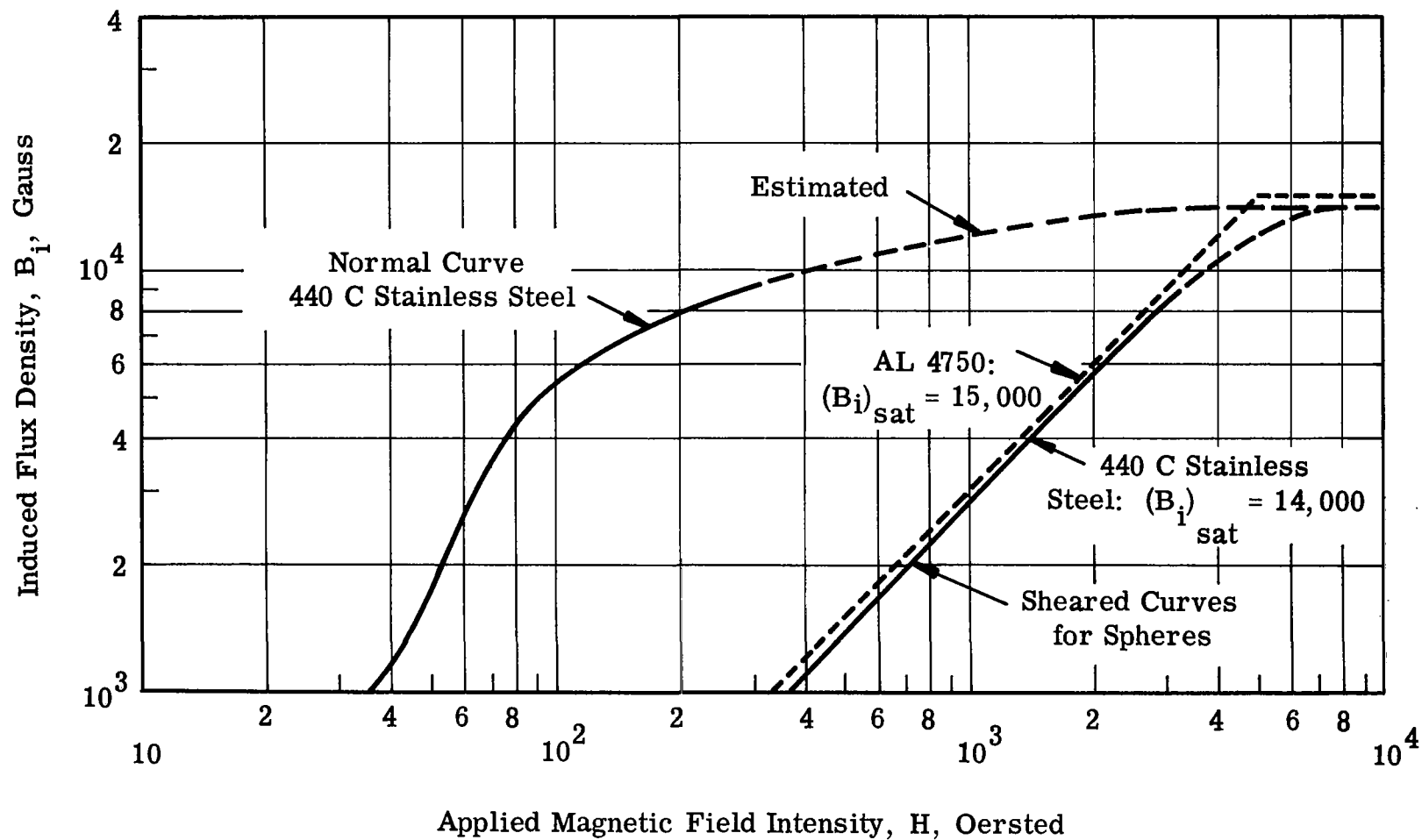


Figure 1. Normal and Sheared Magnetization Curves

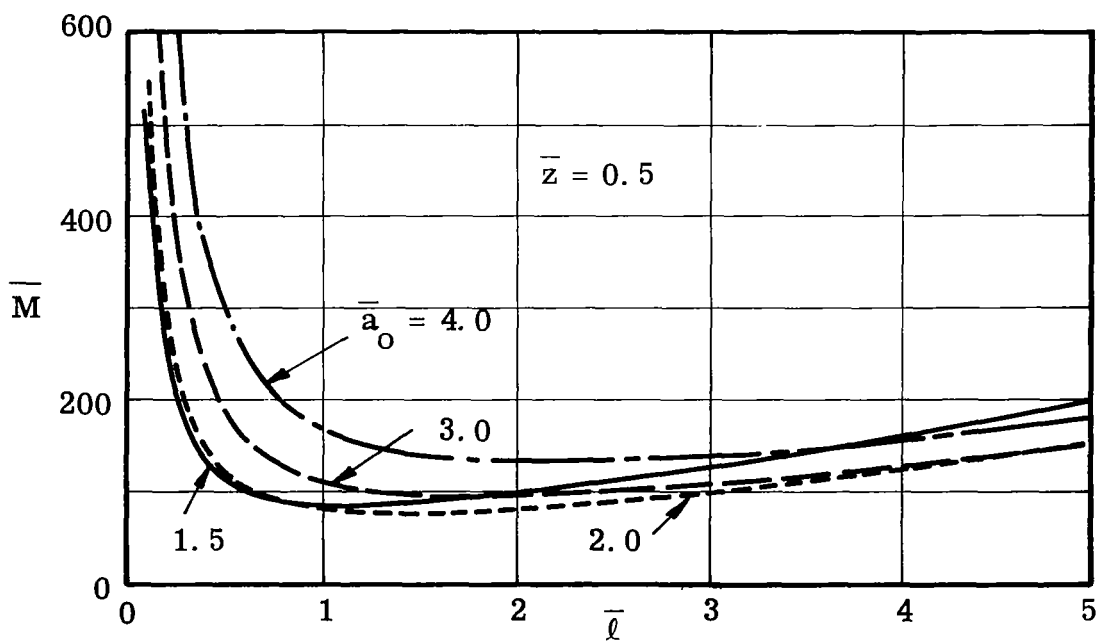
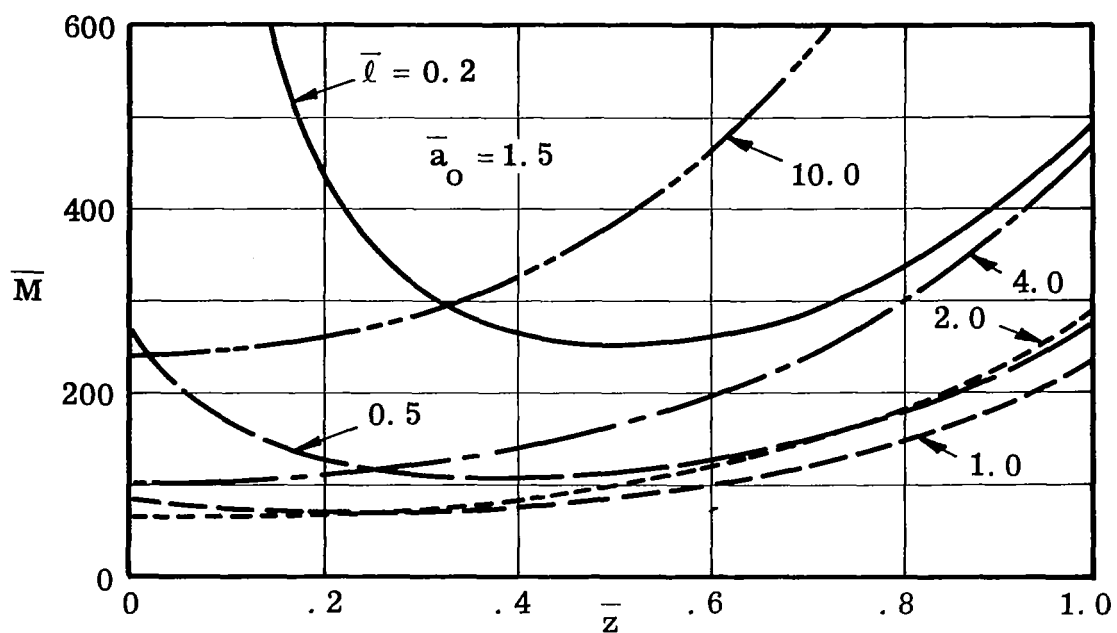


Figure 2. Solenoid Power Factor \bar{M}

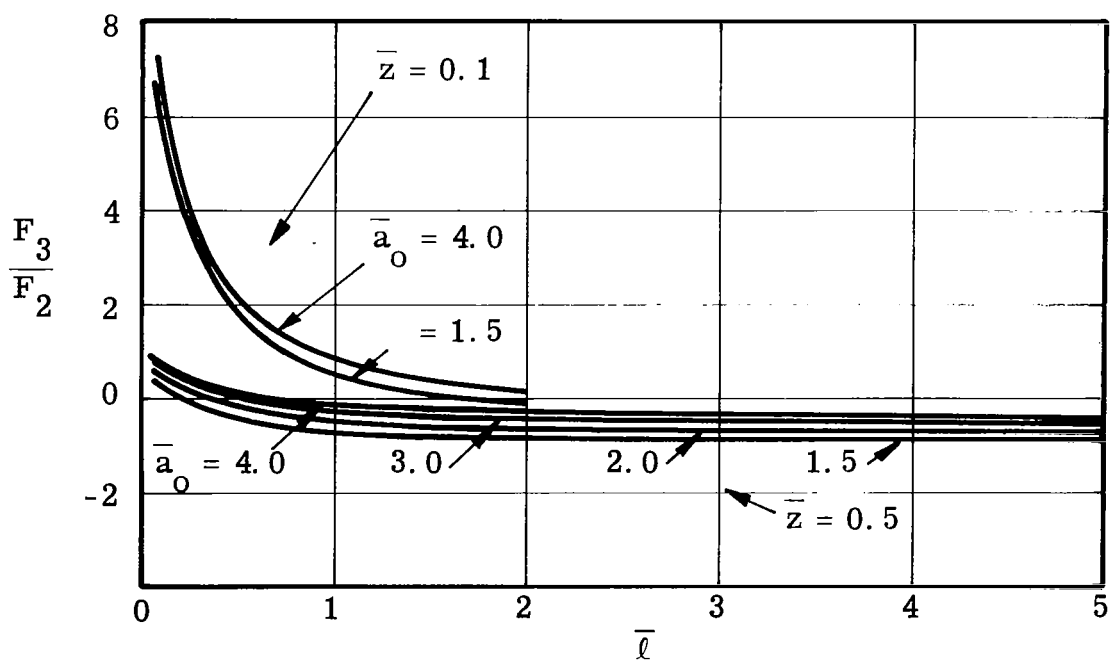
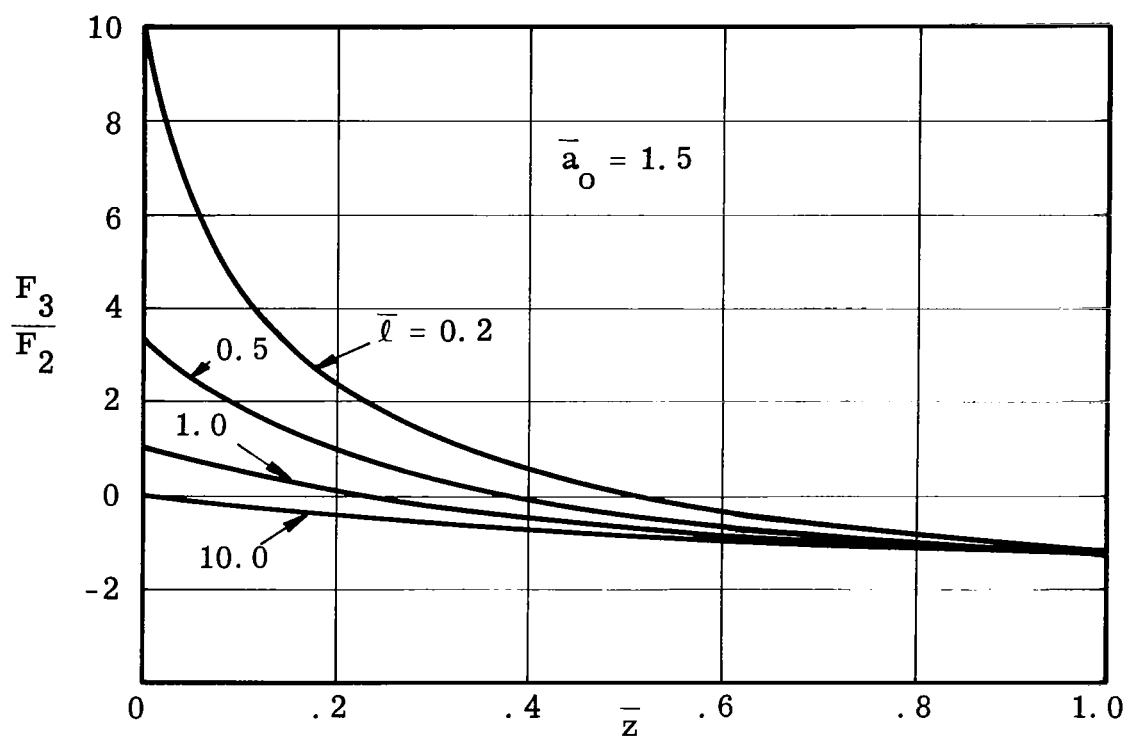


Figure 3. Solenoid F-Factor Ratio F_3/F_2

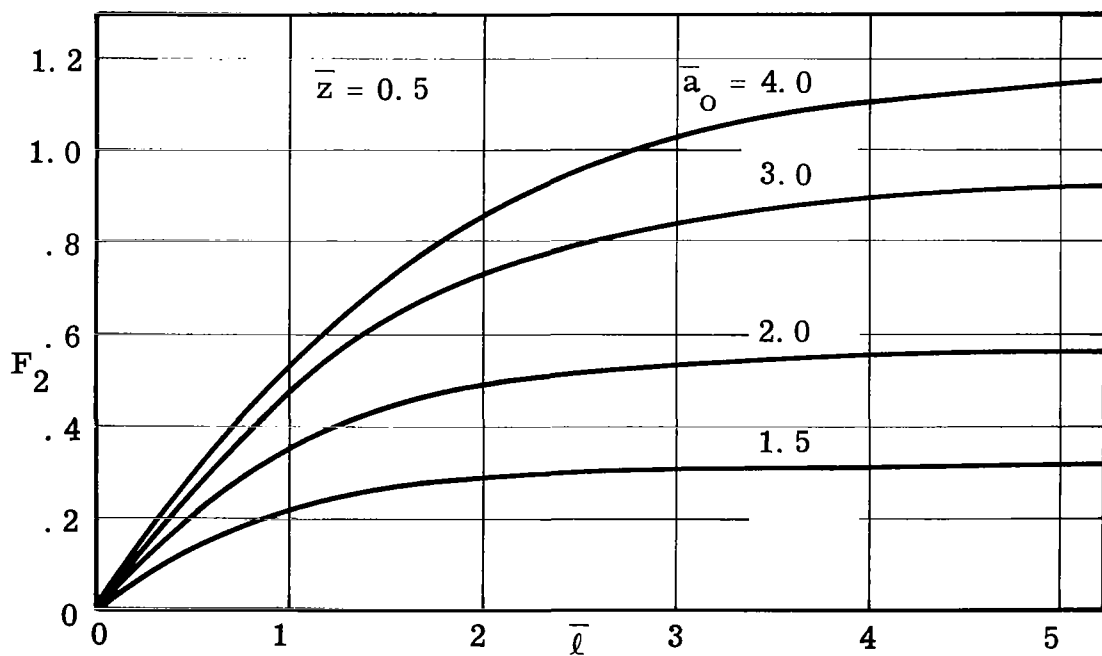
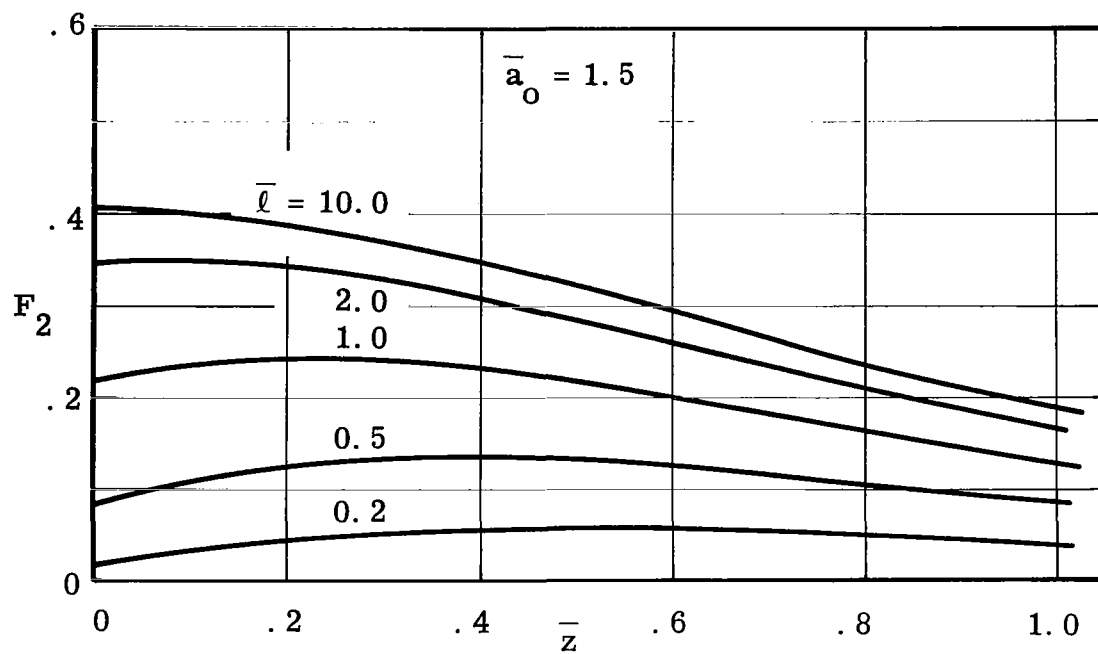


Figure 4. Solenoid F-Factor F_2

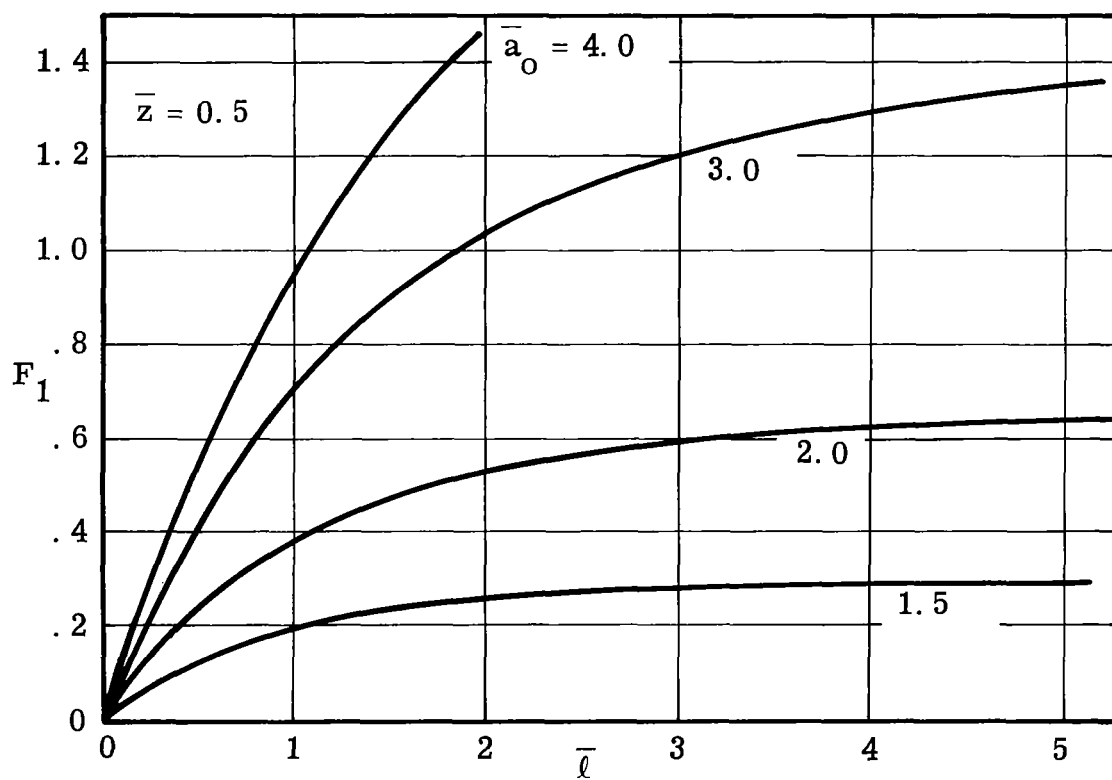
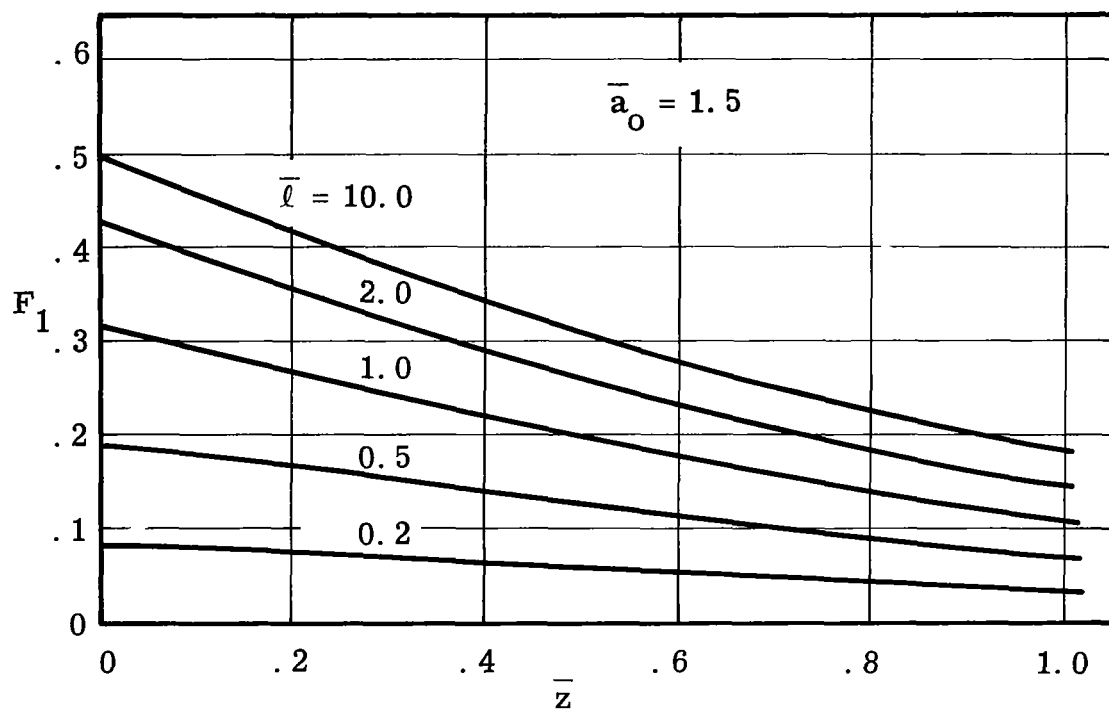


Figure 5. Solenoid F-Factor F_1

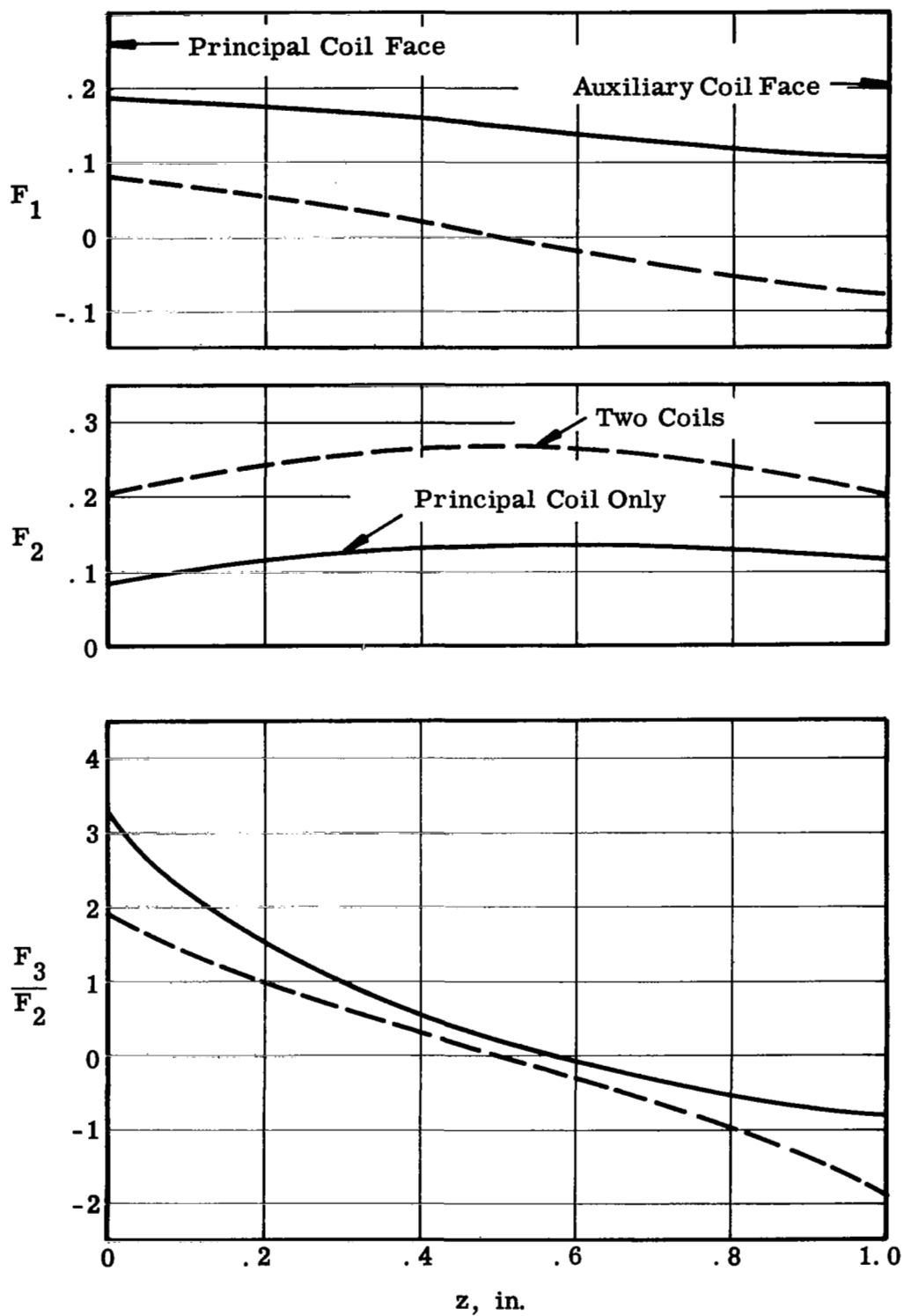


Figure 6. F-Factor Distributions for One and Two Gradient Coil Configurations

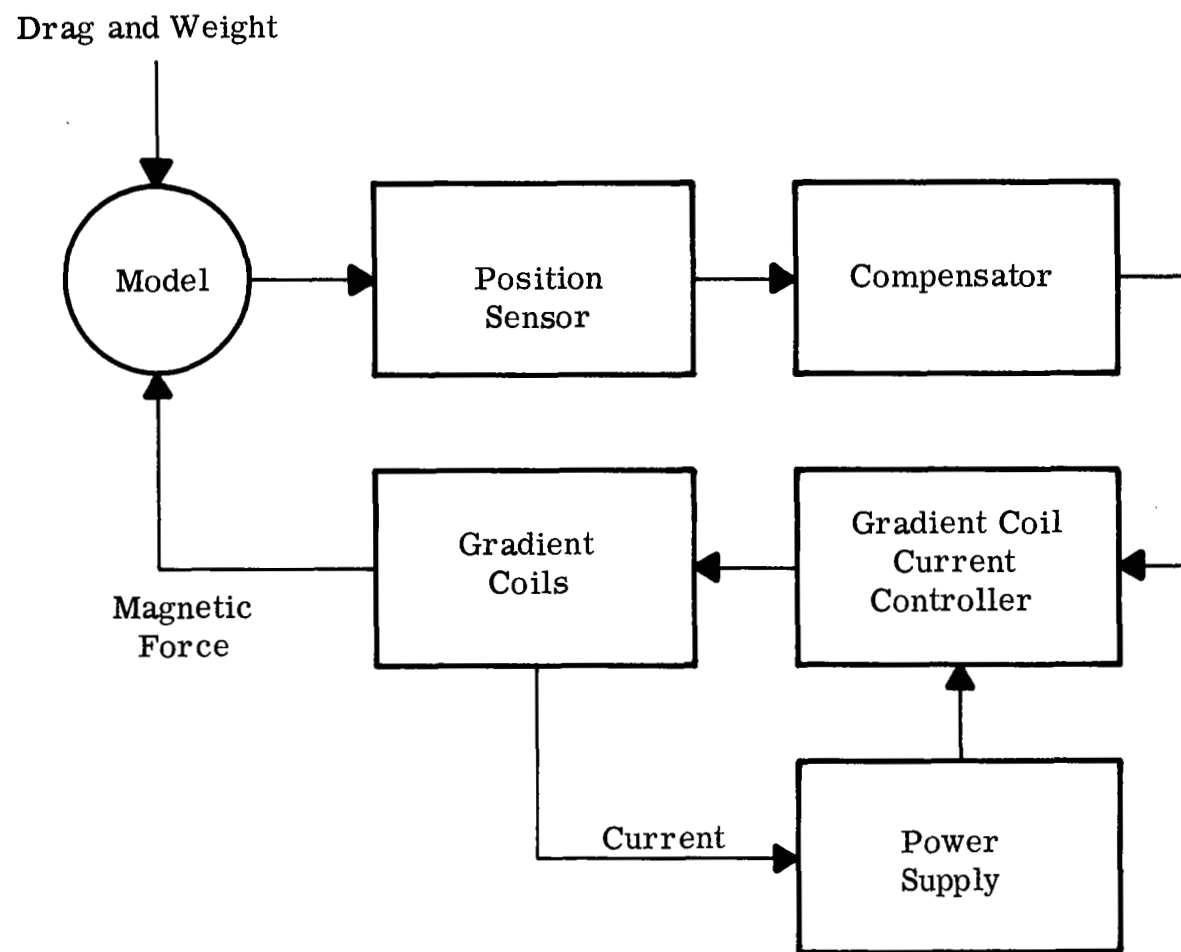


Figure 7. Block Diagram of Magnetic Force Control System.

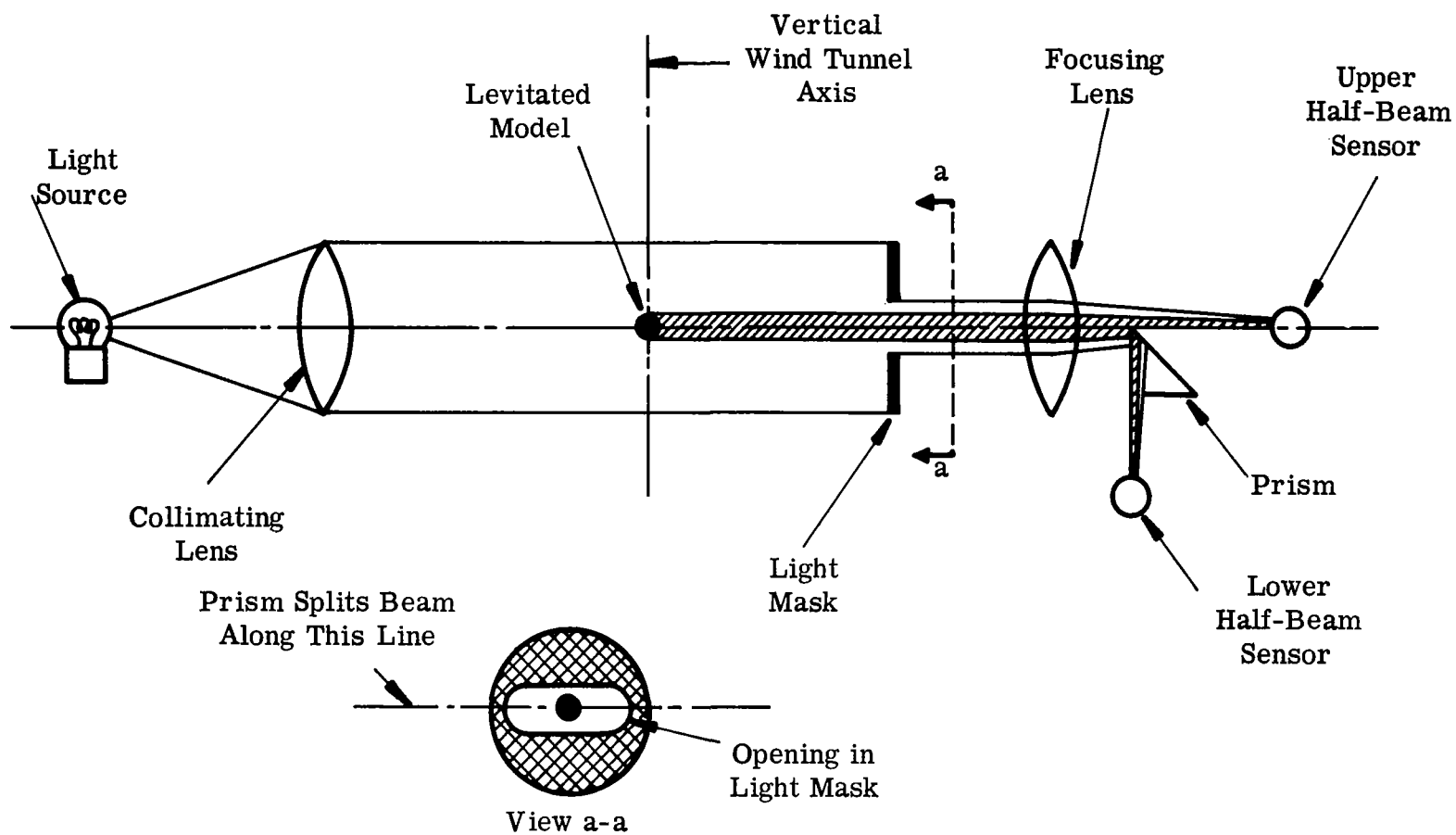


Figure 8. Sketch Showing Model Position Sensor Operation

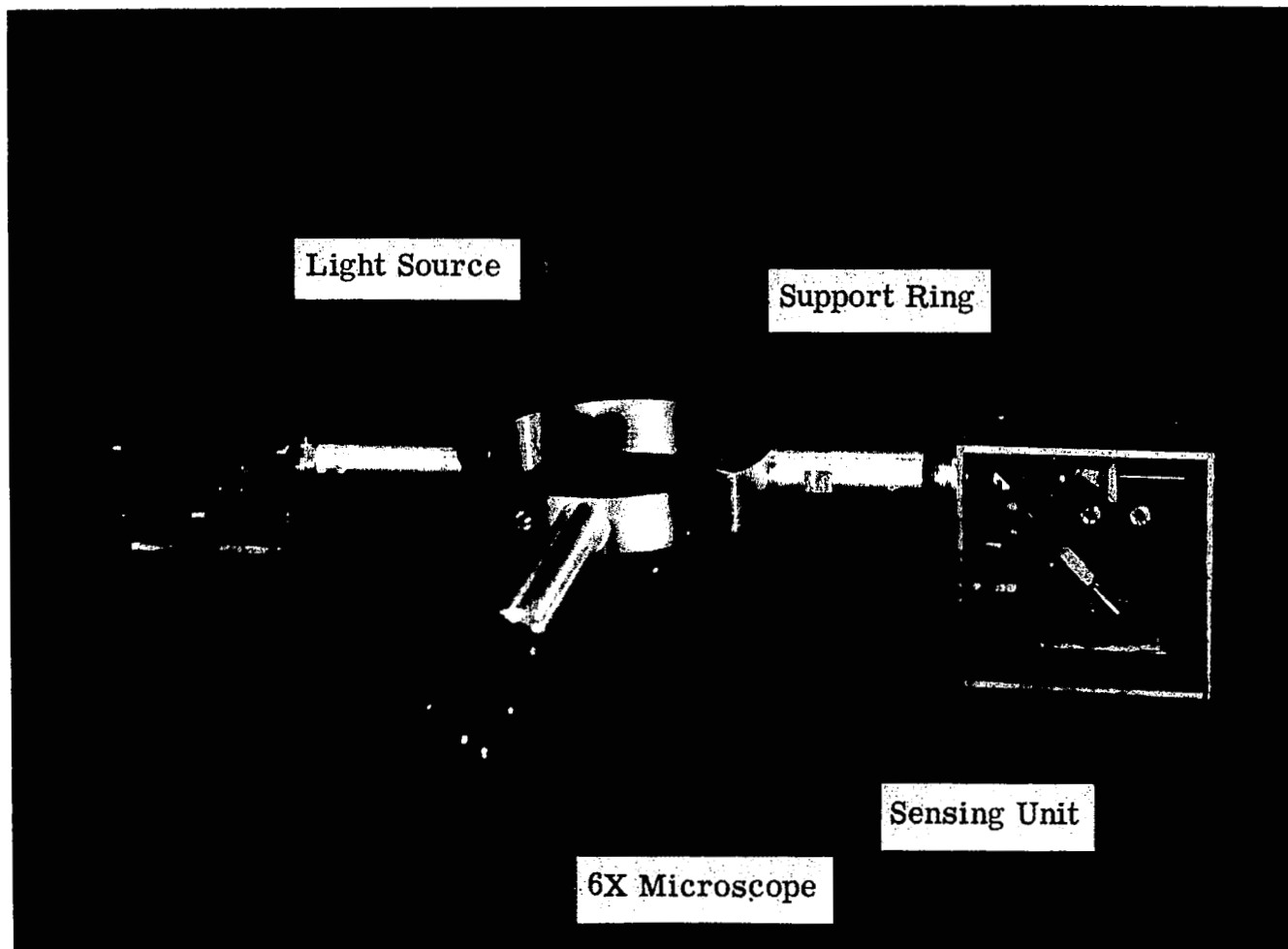


Figure 9. Photograph of Model Position Sensor Assembly.

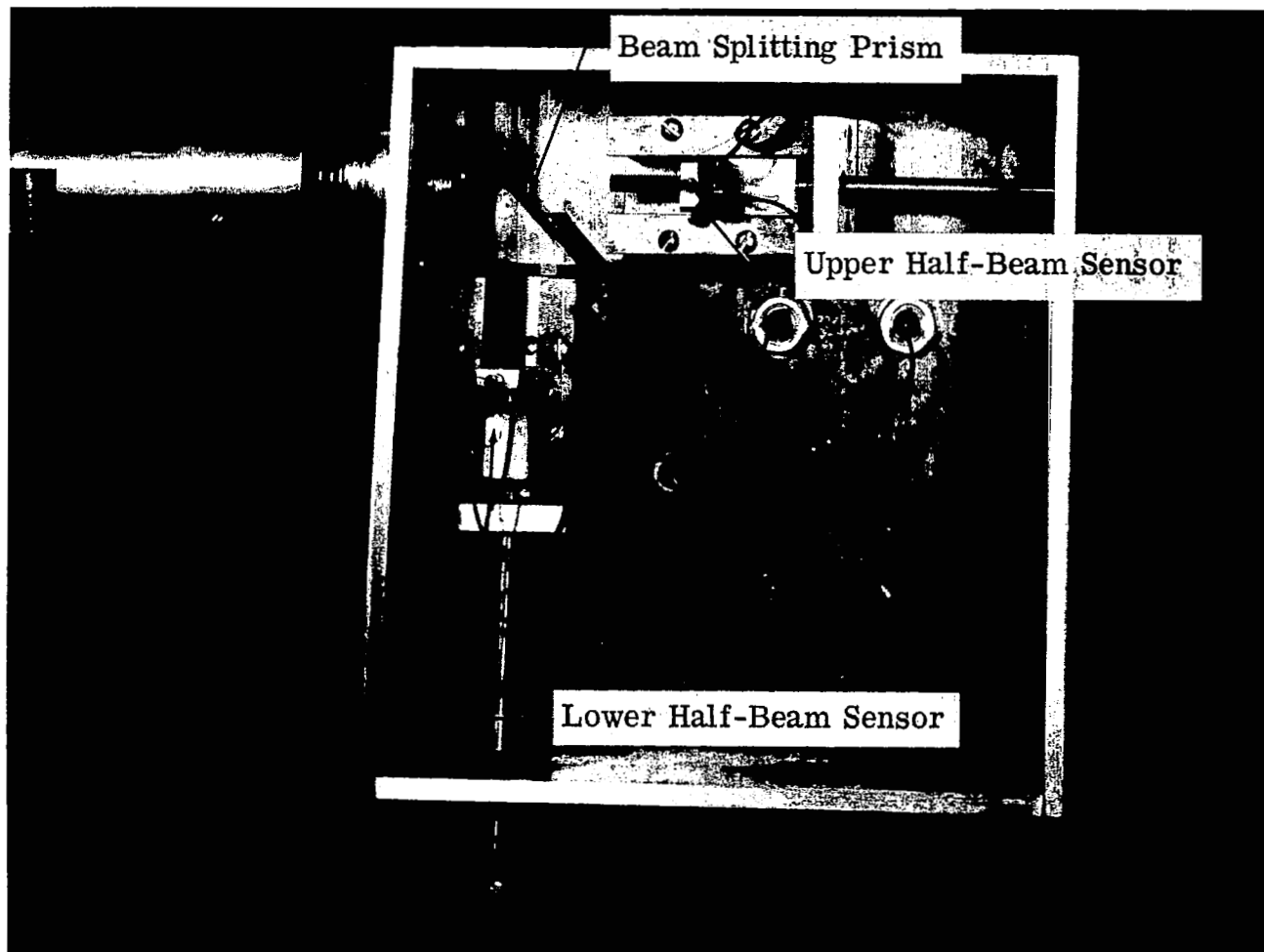
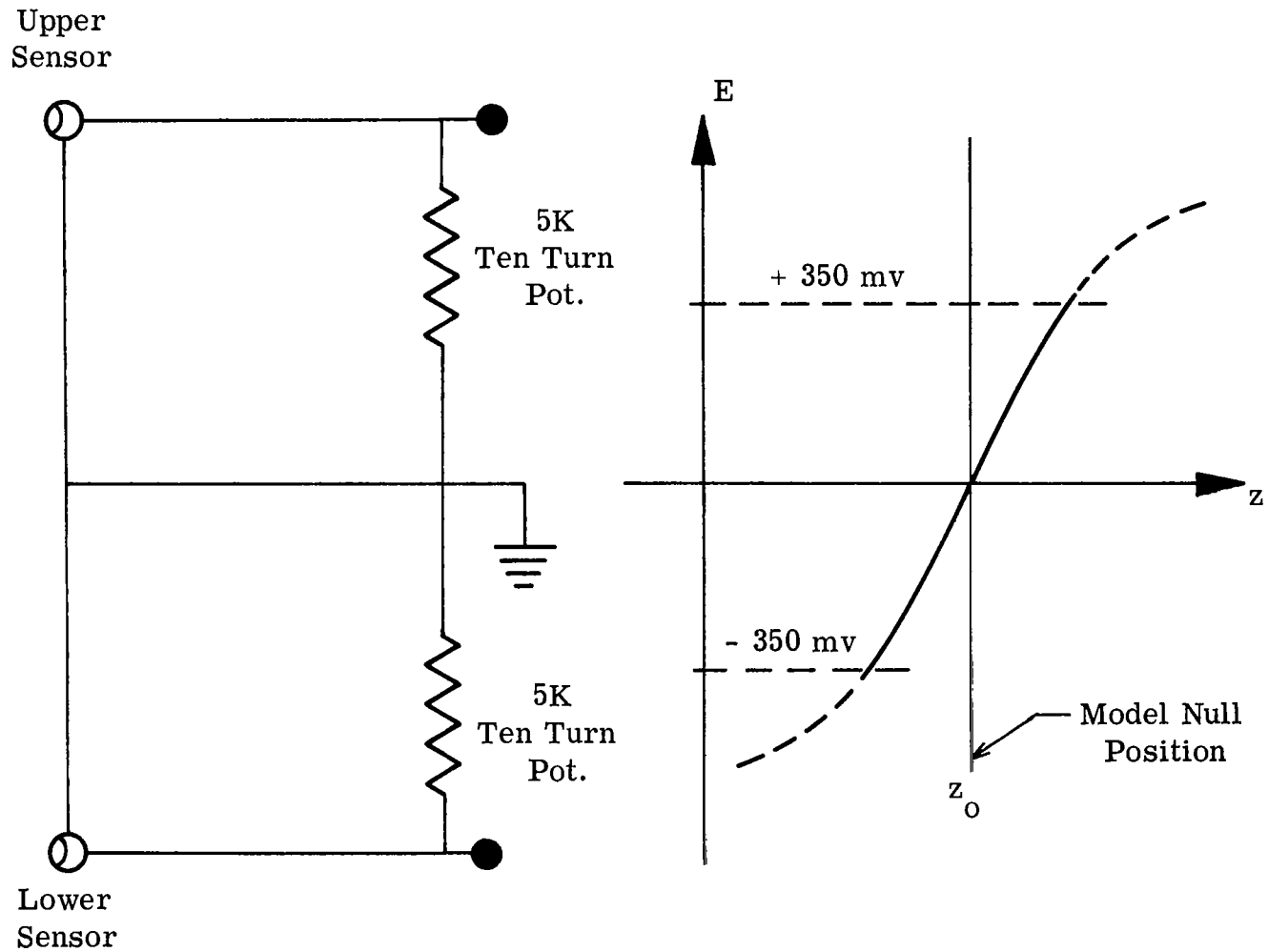


Figure 10. Photograph of Model Position Sensing Unit.



(Sensors are Texas
Instrument LS 221)

Figure 11. Model Position Sensor Circuit and Output Response to Model Motion

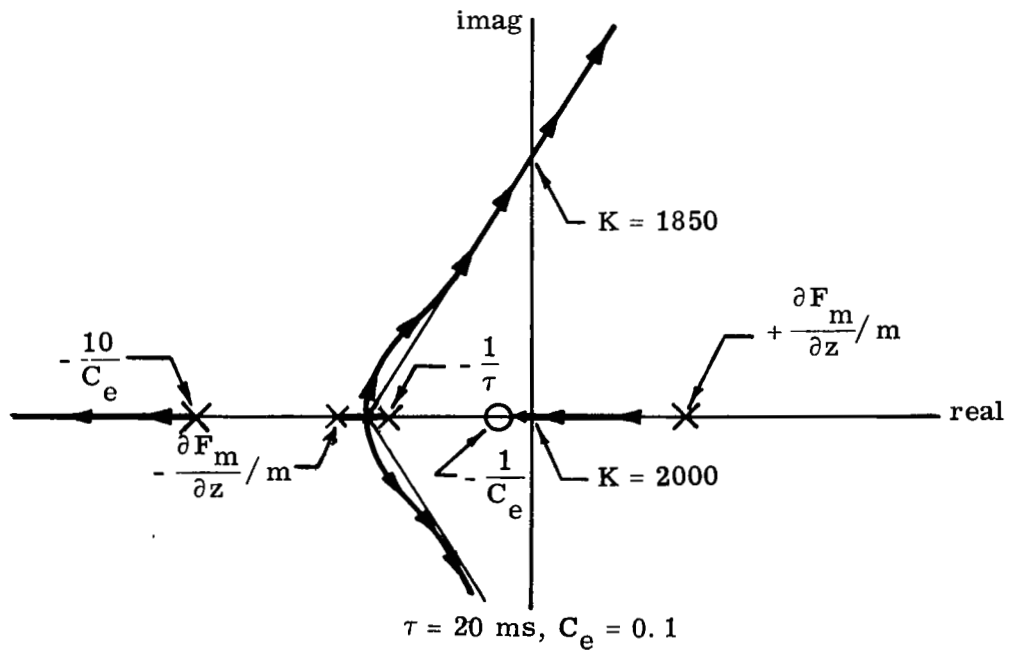
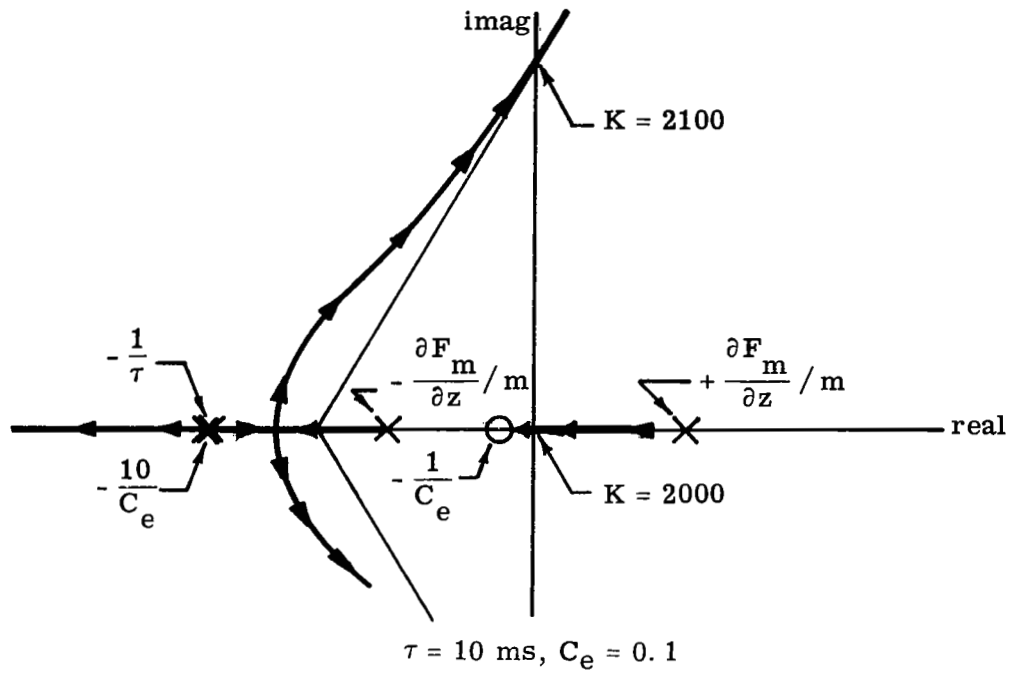
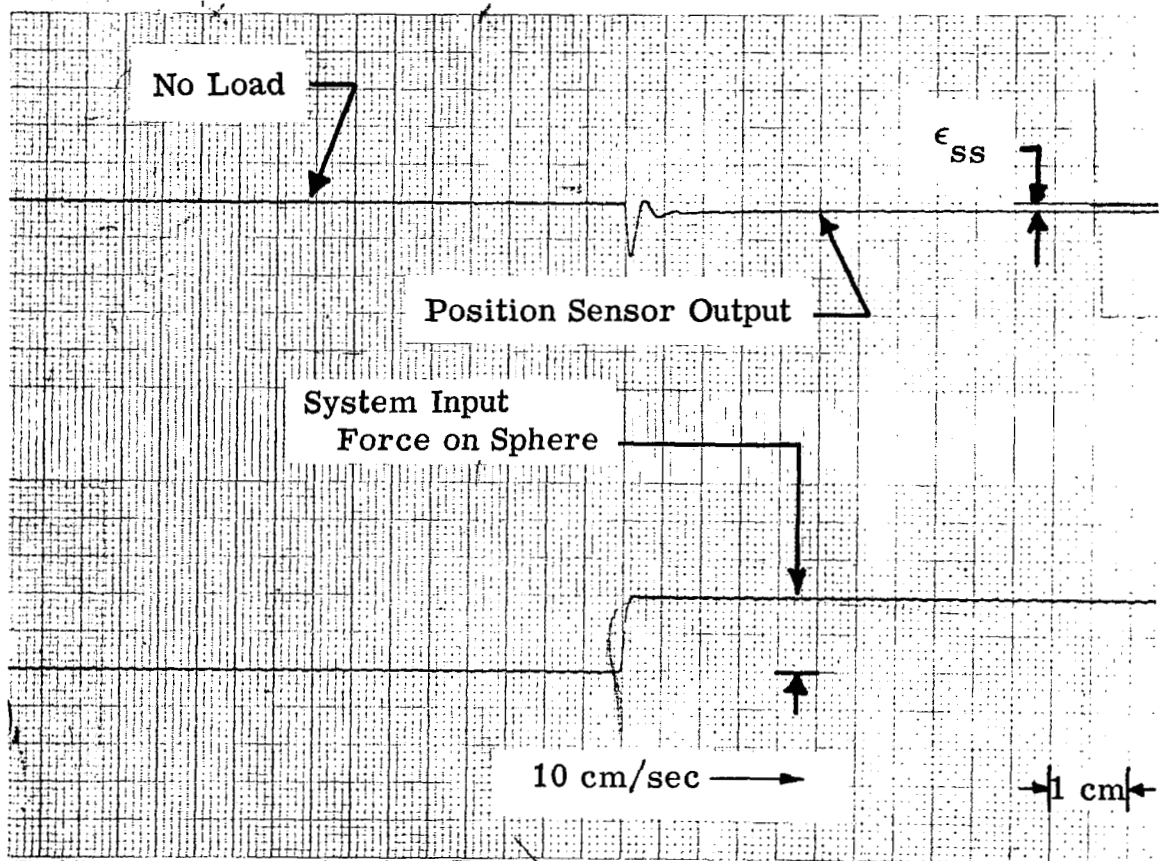
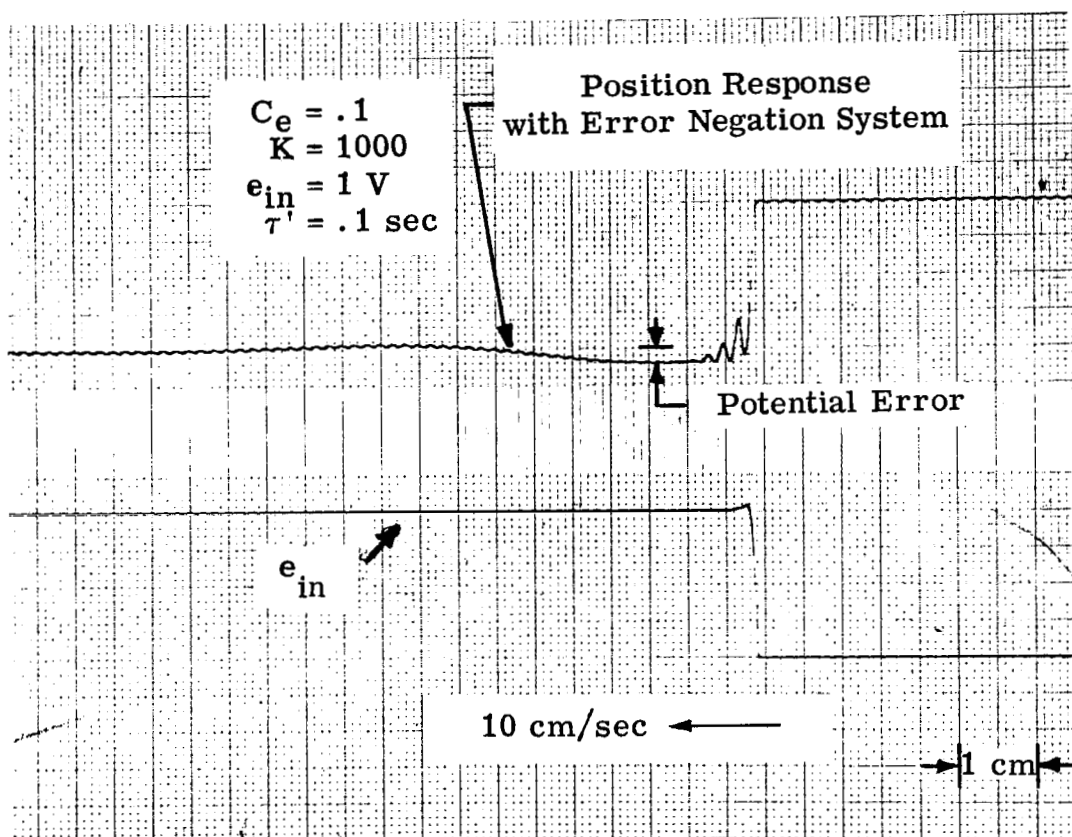


Figure 12. Root-Locus Plots for the Magnetic Control System



(ϵ_{ss} = steady-state error output of position sensor)

Figure 13. Error-Rate Control Simulation Results;
System Response to Step Input.



$$[K = (K_s)(K_{adj})(K_{cc})/0.1 \tau]$$

Figure 14. Response Using an Error Negation Network;
Response to a Step Change in the Position Control.

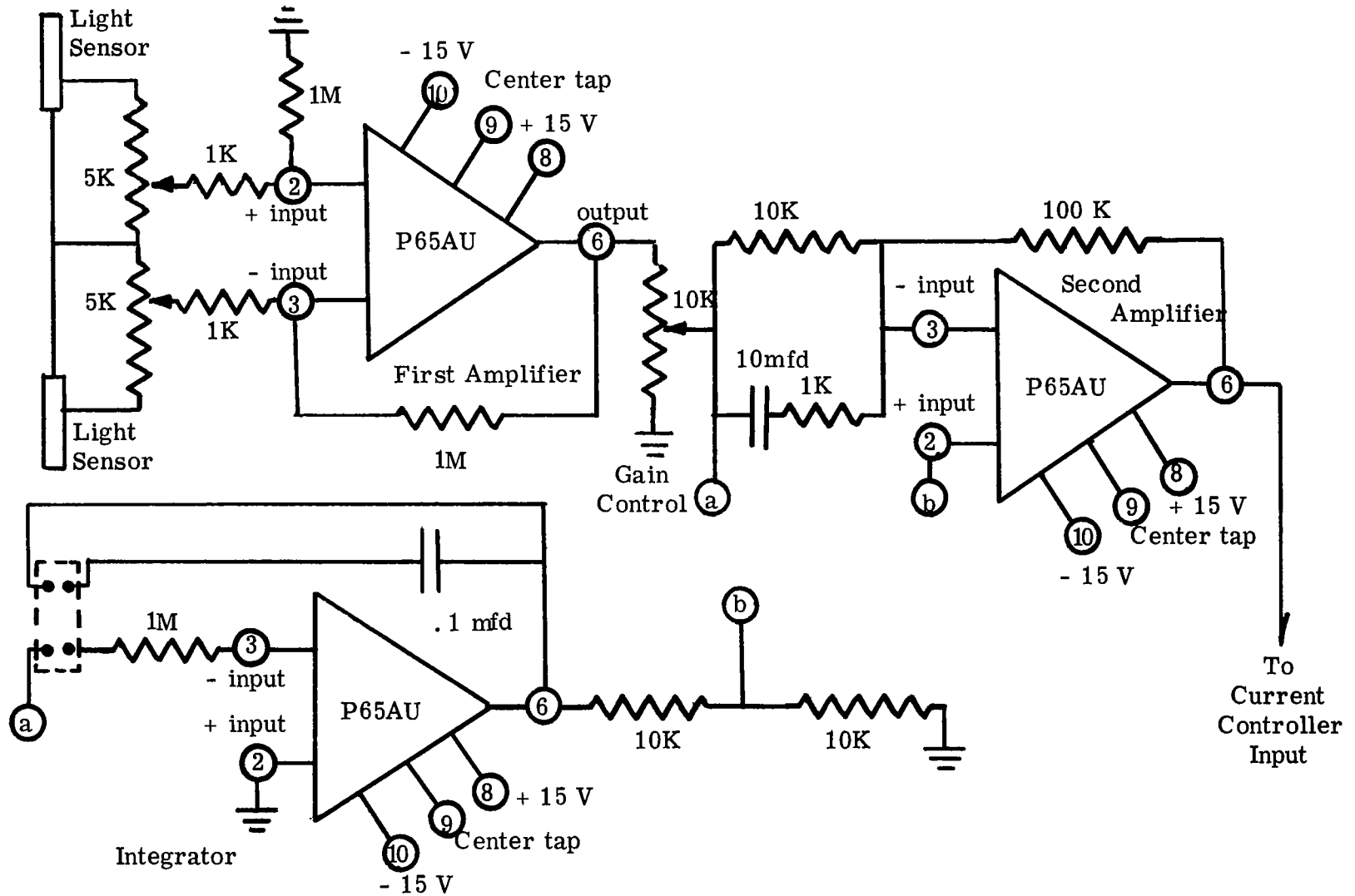


Figure 15. Compensation Unit Circuit

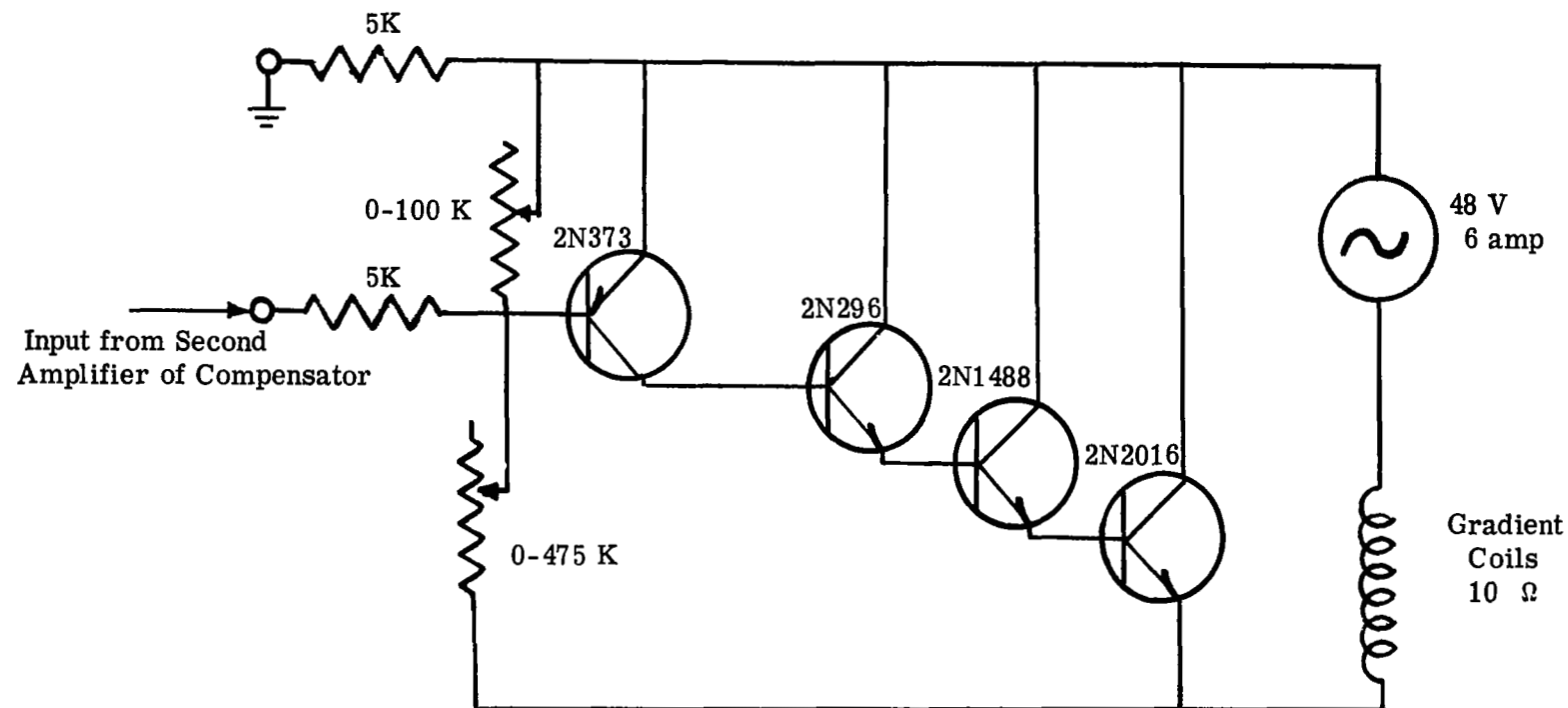


Figure 16. Current Controller Circuit.

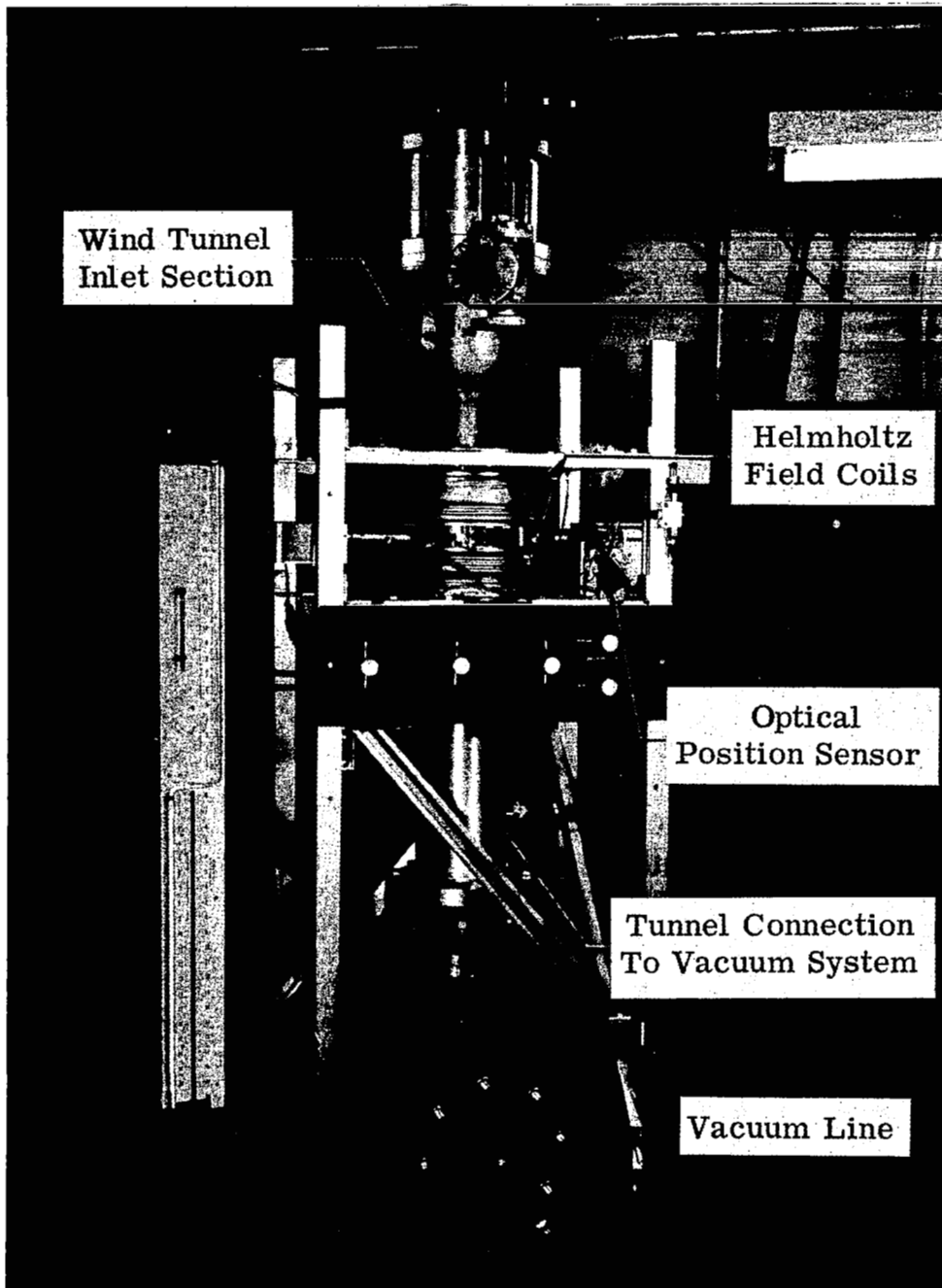


Figure 17. Photograph of Wind Tunnel with Support-and-Balance System Installed.

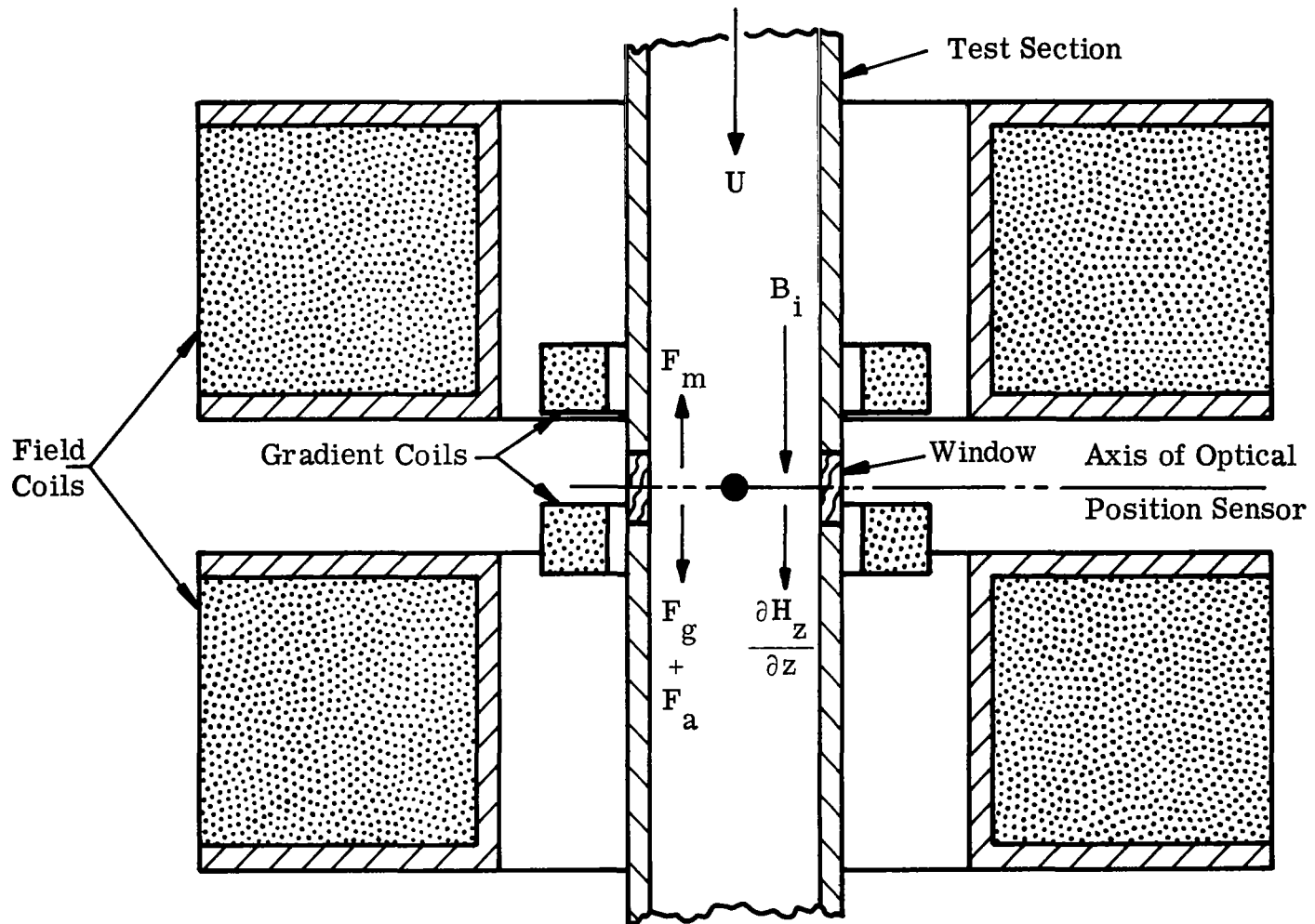
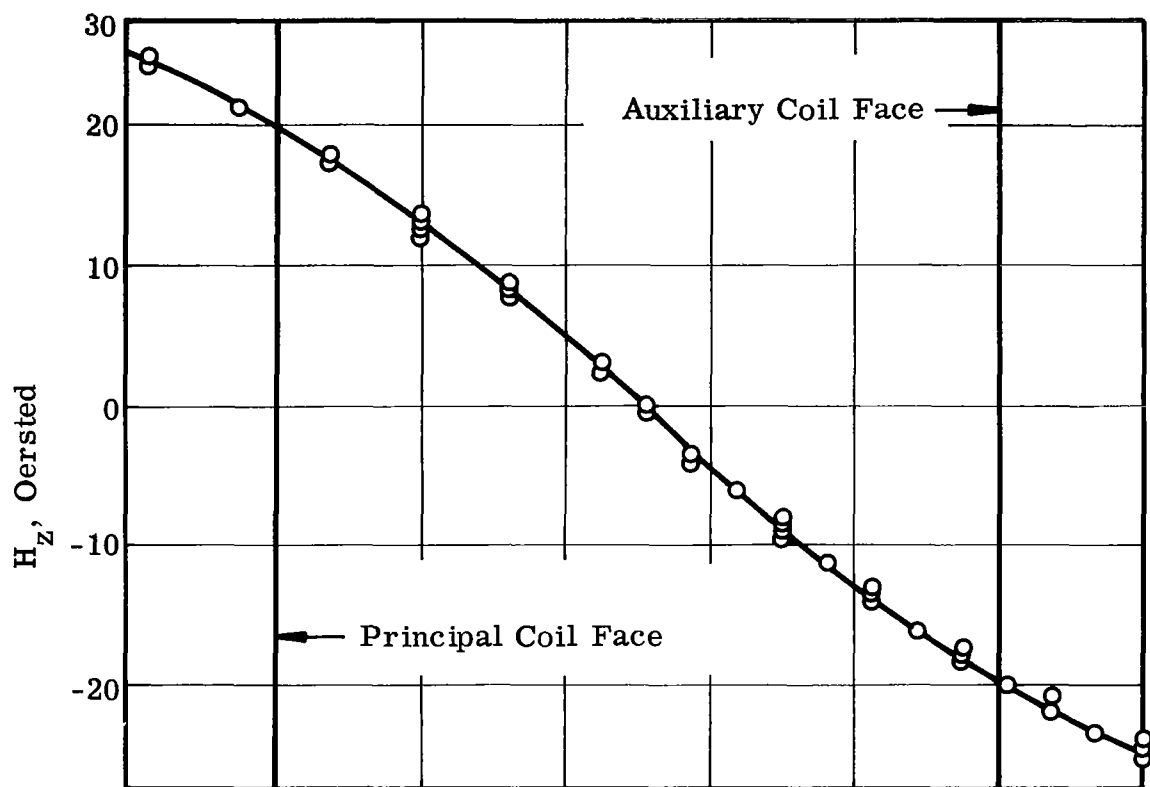


Figure 18. Sketch of Magnetic Coils and Test Section Assembly.



Note: Coil Current = 0.8 amperes for both curves.

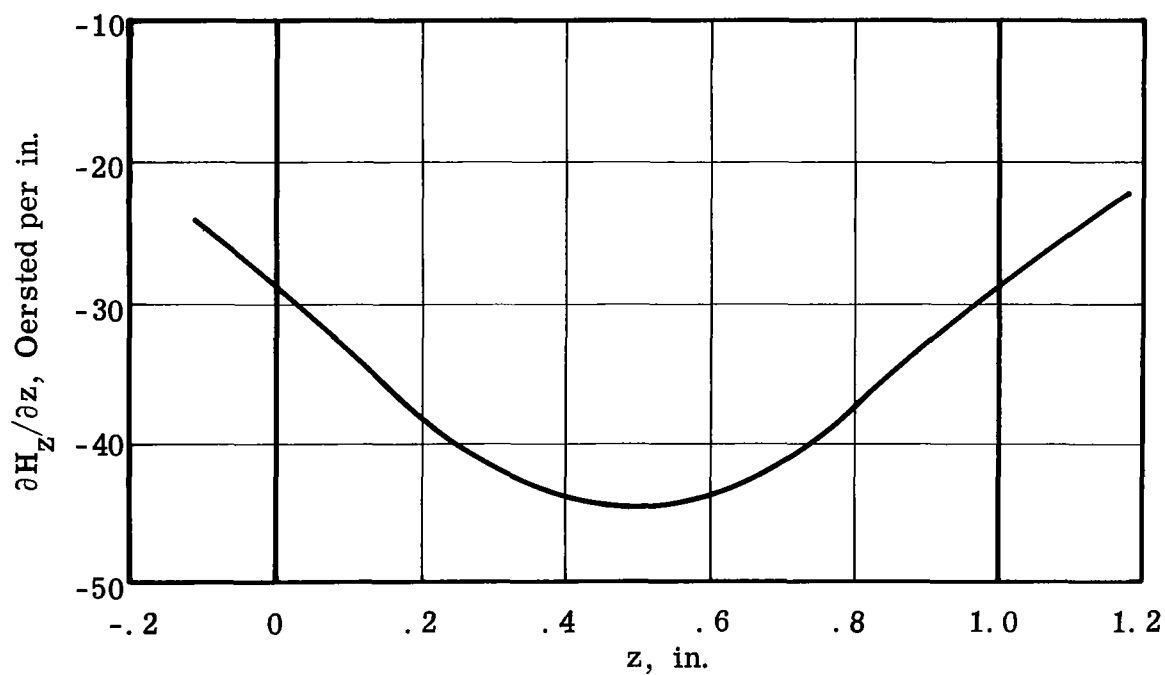


Figure 19. Gradient Coil Calibration: H_z and $\partial H_z / \partial z$

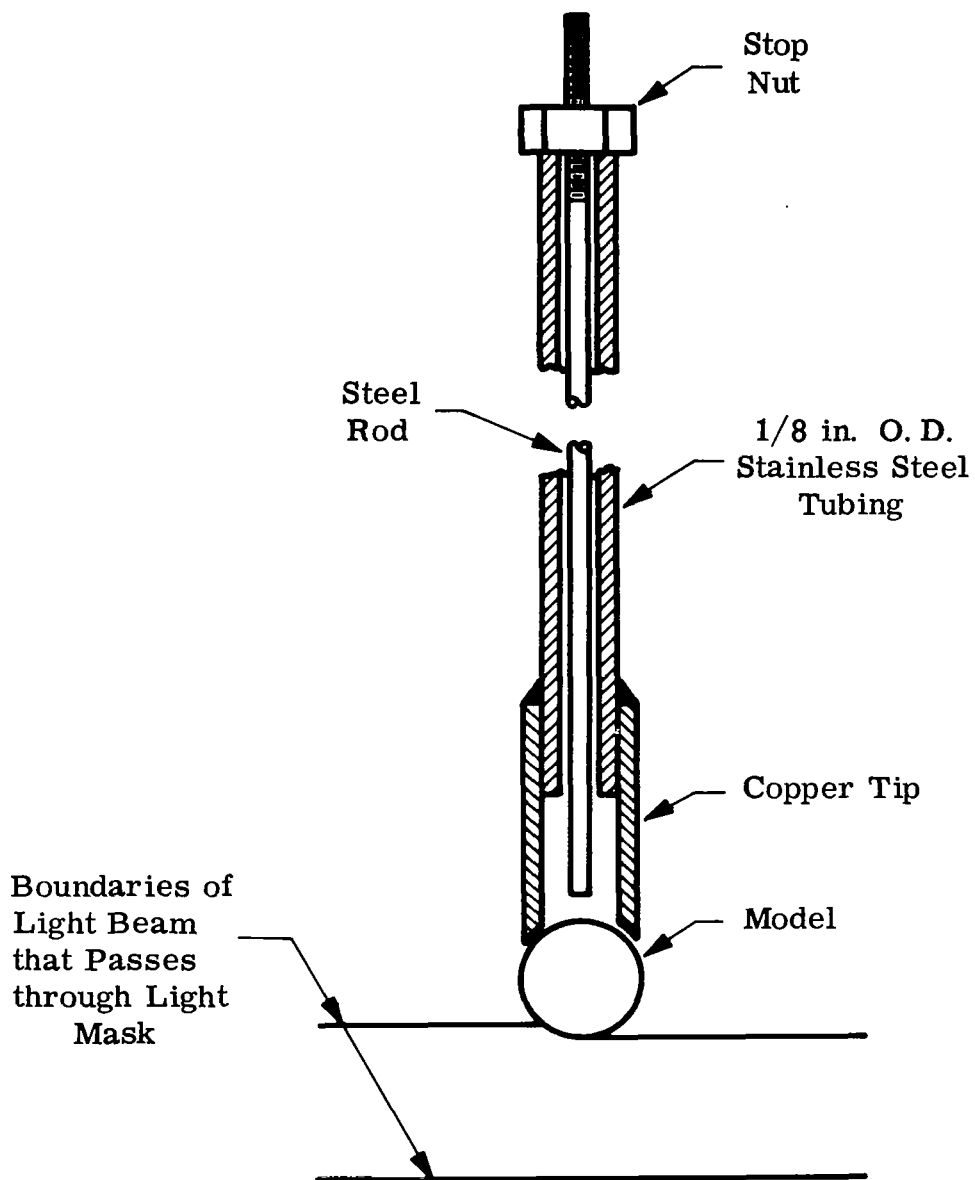


Figure 20. Sketch of Magnetic Model Insertion Probe

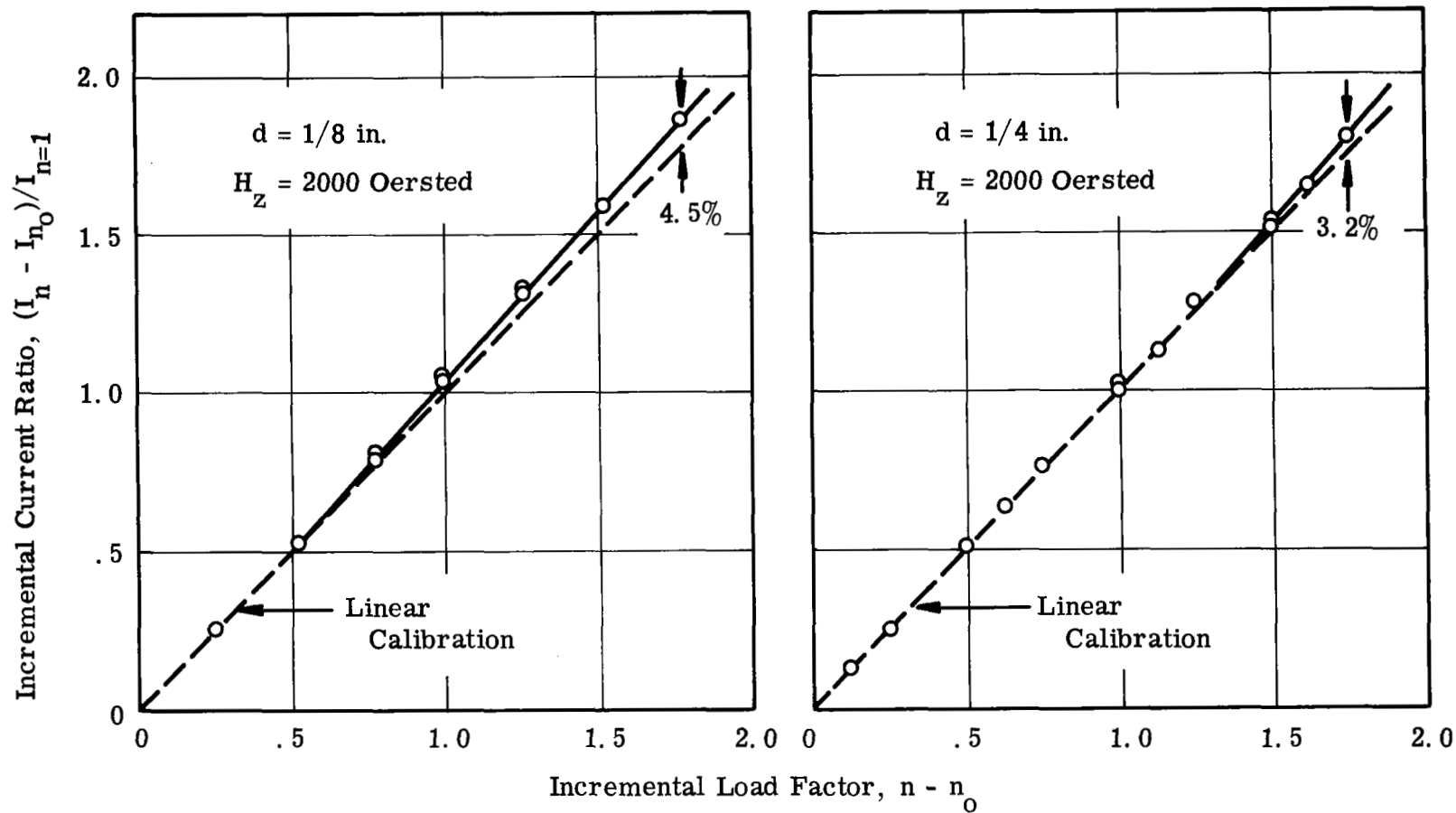
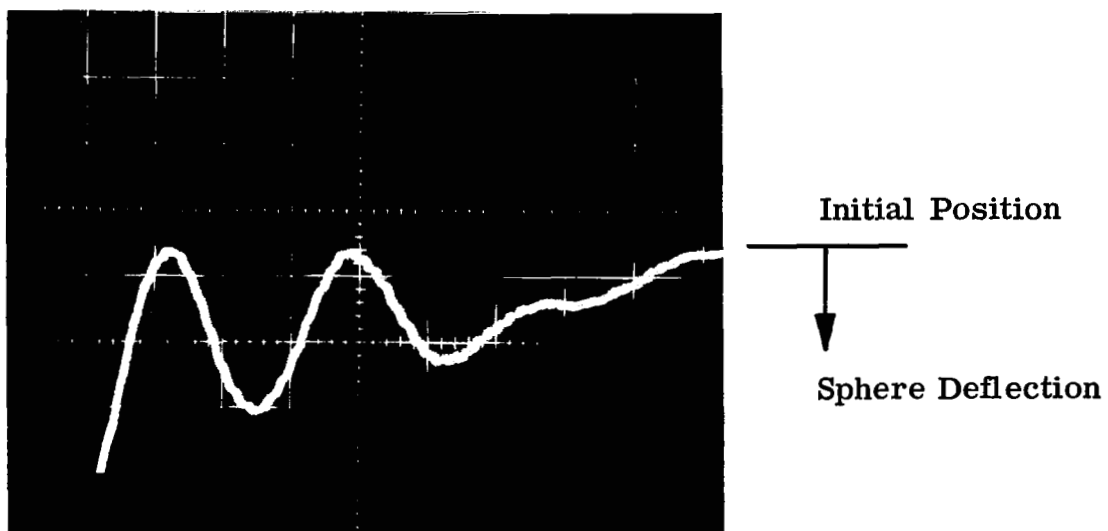
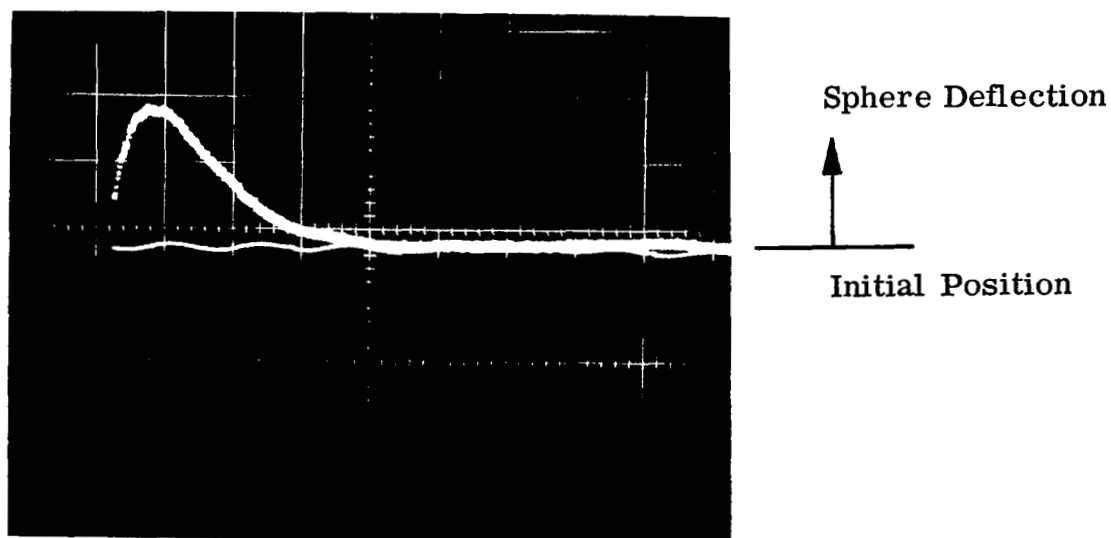


Figure 21. Load Calibration of Magnetic Support-and-Balance System



22(a) Impulse Response
15 ms/cm Sweep →



22(b) Step Response
200 ms/cm Sweep →

Figure 22. Support System Transient Response

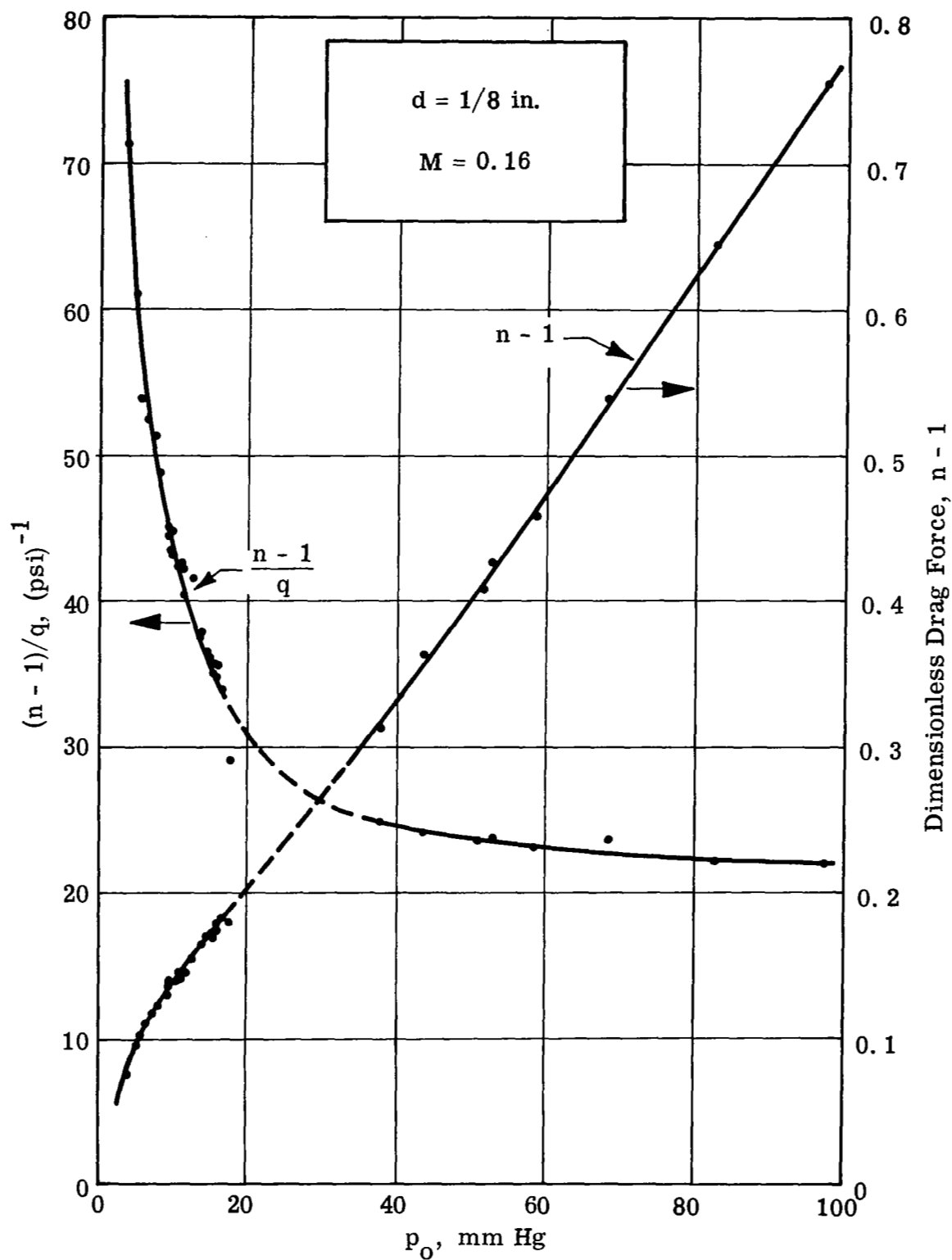


Figure 23. Data from Typical Sphere Drag Test

Appendix A

FORCE ON A FERROMAGNETIC BODY IMMERSED IN THE SYMMETRICAL FIELD OF A SOLENOID

The force on a ferromagnetic body in a non-uniform magnetic field can be written in MKS units as (for example, see Ref. 23)

$$\vec{F} = \mu V (\vec{M} \cdot \nabla) \vec{H} \quad (\text{A-1})$$

where μ = permeability of the medium containing the field (here, assumed to be constant), henry/meter

V = volume of the body, cubic meters

\vec{M} = specific magnetization vector of the body, ampere-turn/meter

\vec{H} = magnetic field vector, ampere-turn/meter

If Eq. (A-1) is expanded using a cylindrical coordinate system and if \vec{i} , \vec{j} , and \vec{k} are taken as the set of orthogonal unit vectors for this coordinate system, then Eq. (A-1) becomes successively

$$\vec{F} = \mu V \left[(M_r \vec{i} + M_\theta \vec{j} + M_z \vec{k}) \cdot \left(\frac{\partial}{\partial r} \vec{i} + \frac{1}{r} \frac{\partial}{\partial \theta} \vec{j} + \frac{\partial}{\partial z} \vec{k} \right) \right] \vec{H}$$

$$\vec{F} = \mu V \left(M_r \frac{\partial}{\partial r} + \frac{1}{r} M_\theta \frac{\partial}{\partial \theta} + M_z \frac{\partial}{\partial z} \right) (H_r \vec{i} + H_\theta \vec{j} + H_z \vec{k})$$

The components of this force then become

$$F_r = \mu V \left(M_r \frac{\partial H_r}{\partial r} + \frac{1}{r} M_\theta \frac{\partial H_r}{\partial \theta} + M_z \frac{\partial H_r}{\partial z} \right)$$

$$F_{\theta} = \mu V \left(M_r \frac{\partial H_{\theta}}{\partial r} + \frac{1}{r} M_{\theta} \frac{\partial H_{\theta}}{\partial \theta} + M_z \frac{\partial H_{\theta}}{\partial z} \right)$$

$$F_z = \mu V \left(M_r \frac{\partial H_z}{\partial r} + \frac{1}{r} M_{\theta} \frac{\partial H_z}{\partial \theta} + M_z \frac{\partial H_z}{\partial z} \right)$$

If the problem is restricted to symmetrical fields of co-axial solenoids, no tangential components of either the magnetization or field vectors will exist, i. e. ,

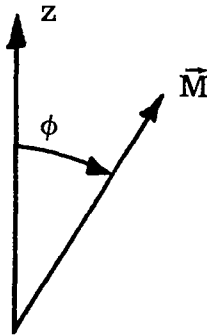
$$M_{\theta} \equiv 0 \quad , \quad H_{\theta} \equiv 0$$

With this important restriction, the magnetic force components become

$$F_r = \mu V \left(M_r \frac{\partial H_r}{\partial r} + M_z \frac{\partial H_r}{\partial z} \right) \quad (A-2a)$$

$$F_z = \mu V \left(M_r \frac{\partial H_z}{\partial r} + M_z \frac{\partial H_z}{\partial z} \right) \quad (A-2b)$$

Further, if ϕ is taken as the angle between the magnetization vector \vec{M} and the positive z-axis,



the radial and axial components of \vec{M} can be written as

$$M_r = M \sin \phi$$

$$M_z = M \cos \phi$$

where M is the magnitude of \vec{M} . Then Eq. (A-2) becomes

$$F_r = \mu VM \left(\frac{\partial H_r}{\partial r} \sin \phi + \frac{\partial H_r}{\partial z} \cos \phi \right) \quad (\text{A-3a})$$

$$F_z = \mu VM \left(\frac{\partial H_z}{\partial r} \sin \phi + \frac{\partial H_z}{\partial z} \cos \phi \right) \quad (\text{A-3b})$$

Finally, if the problem is restricted to the neighborhood of the axis of the solenoidal system so that

$$\phi \cong 0$$

Eq. (A-3) can be written as*

*This is, of course, exactly true on the axis of a co-axial solenoidal system. It is also a very good approximation for F_z in the neighborhood of the axis because not only will ϕ be small near the axis but also because $\partial H_z / \partial r$ is a linear function of r near the axis and is zero on the axis. The situation is not so clear in the case of F_r . $\partial H_r / \partial r$ has a finite and constant value in the neighborhood of the axis and hence $(\partial H_r / \partial r) \sin \phi$ varies directly as ϕ there. $\partial H_r / \partial z$ varies linearly with r near the axis. Therefore both terms in F_r will be small near the axis and it is possible they will be of the same order in this region; the possibility depends on the rate at which ϕ increases with distance away from the axis. Of course, if \vec{M} can be kept very nearly parallel to the axis (i. e., $\phi \cong 0$) over some region near the axis, the approximation for $\partial F_r / \partial r$ will be good there.

$$F_r \cong \mu VM \frac{\partial H_r}{\partial z} \cos \phi \quad (A-4a)$$

$$F_z \cong \mu VM \frac{\partial H_z}{\partial z} \cos \phi \quad (A-4b)$$

The $\cos \phi$ factor has been retained in these equations to indicate that the sign of the forces can be changed by changing the direction of the magnetization vector; e.g., aligning \vec{M} with the negative z-axis produces a change in sign of both F_r and F_z .

From Eq. (A-4), the effective spring constants or static stability derivatives for the r and z directions are found directly as

$$\frac{\partial F_r}{\partial r} = \mu VM \frac{\partial}{\partial r} \left(\frac{\partial H_r}{\partial z} \right) \cos \phi \quad (A-5a)$$

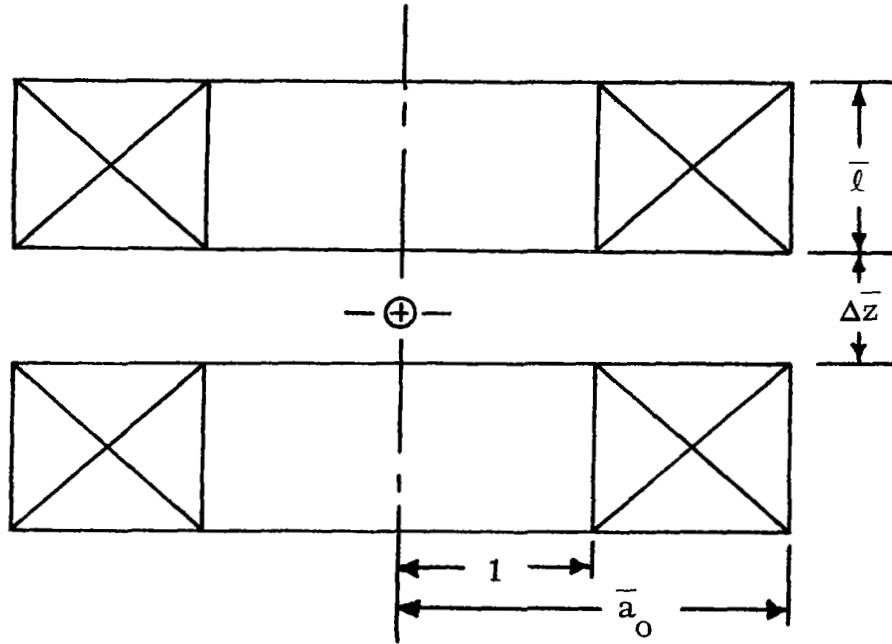
$$\frac{\partial F_z}{\partial z} = \mu VM \frac{\partial^2 H_z}{\partial z^2} \cos \phi \quad (A-5b)$$

Note that the sign of these derivatives also can be controlled by the orientation of \vec{M} .

Appendix B

HELMHOLTZ FIELD COIL DESIGN

The generation of uniform magnetic fields by air-cored coils with finite winding areas has been analyzed by Franzen, Ref. 26. One simple configuration that produces a uniform field is the single Helmholtz coil pair. The geometry of a typical Helmholtz pair is shown in the following sketch. Note that the pertinent dimensions have been reduced by the inner radius of the coils; e.g., $\bar{a}_o = a_o / (a_i)_o$.



Note: All dimensions have been non-dimensionalized by the inner radius of the coils, $(a_i)_o$.

Helmholtz Pair Geometry

A fourth-order field is produced in the vicinity of the geometric center of the Helmholtz pair; i. e. , in the expansion of the field, in the neighborhood of the center, in terms of the successive derivatives of the axial field at the center, the first non-vanishing term is of fourth order. Franzen has solved analytically for the geometry of a Helmholtz pair with a finite winding area. In terms of the geometry shown in the above sketch, the Helmholtz condition is obtained if the following geometrical relationships are satisfied.

$$\bar{\ell} = 0.928 (\bar{a}_0 - 1)$$

$$\Delta \bar{z} = 1.428 - 0.428 \bar{a}_0$$

These relationships are plotted in Fig. B-1 as an aid in making quick design estimates.

Two important factors affecting the Helmholtz coil pair design are the field strength produced and the power required to produce it. Expressions for field strength, and the power required to produce it, on the axis of a coil and at some distance z from the coil face, can be written in the form²⁷

$$H_z = \frac{1}{2} J (a_1)_0 F_1$$

and

$$P = \frac{4\rho_c}{\alpha} (a_1)_0^2 H_z^2 \bar{H}$$

where F_1 and \bar{H} are nondimensional factors that depend only on the non-dimensional geometry of the coil and axial point \bar{z} and not on the scale of the configuration. The configuration scale is accounted for by the inner coil radius $(a_1)_0$. Values of F_1 and \bar{H} are shown in Fig. B-2 for the Helmholtz coil pair geometry. It must be noted that the F_1 and \bar{H} values shown in Fig. B-2 are for one coil only. That is, they can be used to determine the field contribution of one coil alone (one-half of the total field) and the power consumed by that coil.

$$\bar{\ell} = 0.928 (\bar{a}_o - 1)$$

$$\Delta \bar{z} = 1.428 - 0.428 \bar{a}_o$$

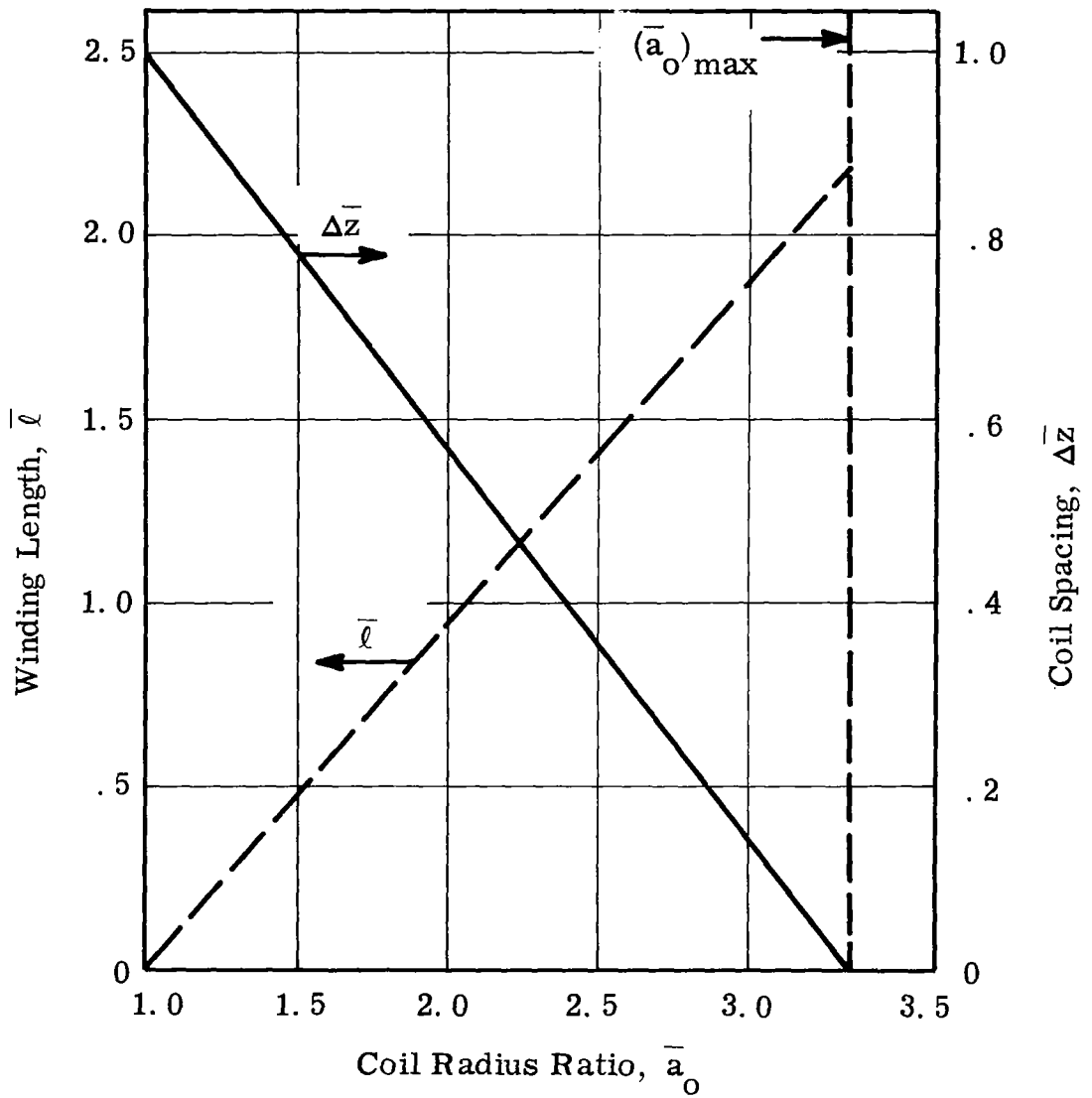
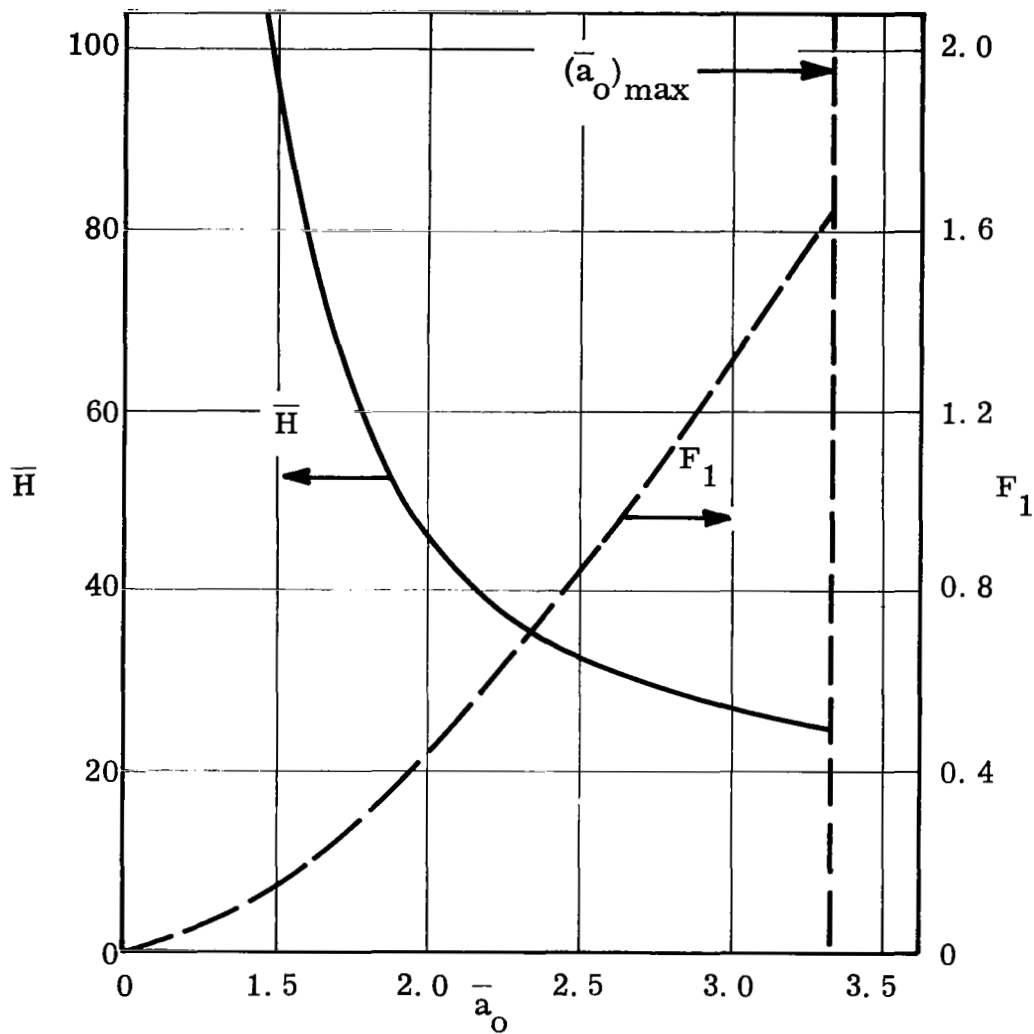


Figure B-1. Helmholtz Pair Geometry



Note: These factors apply to only one coil of the pair.

Figure B-2. Helmholtz Pair Field and Power Factors.